A new method to constrain the appearance and disappearance of observed jellyfish galaxy tails

Smith, R.; Shinn, J.H.; Tonnesen, S.; Calderón-Castillo, P.; Crossett, J.; Jaffe, Y.L.; … ; Shin, J.

Note: To cite this publication please use the final published version (if applicable).

A New Method to Constrain the Appearance and Disappearance of Observed Jellyfish Galaxy Tails

Rory Smith[1] , Jong-Ho Shinn[2] , Stephanie Tonnesen[3] , Paula Calderón-Castillo[4] , Jacob Crossett[5] , Yara L. Jaffe[5] ,
Ian Roberts[6] , Sean McGee[7] , Koshy George[8] , Benedetta Vulcani[9] , Marco Gullieuszik[9] , Alessia Moretti[9] ,
Bianca M. Poggianti[9] , and Jihye Shin[2]

[1] Departamento de Física, Universidad Técnica Federico Santa María, Vicuña Mackenna 3939, San Joaquín, Santiago de Chile, Chile; rorysmith274@gmail.com
[2] Korea Astronomy and Space Science Institute (KASI), 776 Daedeokdae-ro, Yuseong-gu, Daejeon 34055, Republic of Korea
[3] Center for Computational Astrophysics, Flatiron Institute, 162 5th Ave, New York, NY 10010, USA
[4] Departamento de Astronomía, Universidad de Concepción, Casilla 160-C, Concepción, Chile
[5] Instituto de Física y Astronomía, Universidad de Valparaíso, Avda. Gran Bretaña 1111, Valparaíso, Chile
[6] Leiden Observatory, Leiden University, PO Box 9513, 2300 RA Leiden, The Netherlands
[7] University of Birmingham School of Physics and Astronomy, Edgbaston, Birmingham, B15 2TT, UK
[8] Faculty of Physics, Ludwig-Maximilians-Universität, Scheinerstr 1, Munich, D-81679, Germany
[9] INAF–Astronomical Observatory of Padova, Vicolo dell'Osservatorio 5, I-35122 Padova, Italy

Abstract

We present a new approach for observationally constraining where the tails of Jellyfish (JF) galaxies in groups and clusters first appear and how long they remain visible for with respect to the moment of their orbital pericenter. This is accomplished by measuring the distribution of their tail directions, with respect to their host centers, and their distribution in a projected velocity–radius phase-space diagram. We then model these observed distributions using a fast and flexible approach, where JF tails are painted onto dark matter halos, according to a simple parameterized prescription, before a Bayesian analysis is performed to estimate the parameters. We demonstrate the effectiveness of our approach using observational mocks, then apply it to a known observational sample of 106 JF galaxies, with radio-continuum tails located inside 68 hosts such as groups and clusters. We find that, typically, the radio-continuum tails become visible on first infall, when the galaxy reaches roughly three-quarters of r_{200}, and the tails remain visible for a few hundred Myr after pericenter passage. Lower-mass galaxies in more massive hosts tend to form visible tails further out and their tails disappear more quickly after pericenter. We argue that this indicates that they are more sensitive to ram pressure stripping. With upcoming large-area surveys of JF galaxies in progress, this is a promising new method for constraining the environmental conditions in which visible JF tails exist.

Unified Astronomy Thesaurus concepts: Orbits (1184); Galaxy clusters (584); Galaxy evolution (594); Galaxy tails (2125); Galaxy groups (597); Radio continuum emission (1340); Galaxy dark matter halos (1880)

1. Introduction

For several decades, it has been recognized that galaxies become increasingly deficient in atomic gas (H I) in dense environments, such as clusters or massive groups (Davies & Lewis 1973; Huchtmeier et al. 1976; Haynes & Giovanelli 1986; Solanes et al. 2001; Boselli & Gavazzi 2006), compared to their counterparts in the field (Chamaraux et al. 1980; Solanes et al. 1996; Toribio et al. 2011; Dénes et al. 2014; Jones et al. 2018). The loss of H I gas is believed to be of significance for galaxy evolution (see Cortese et al. 2021 for a recent review), and a net reduction in galaxy star formation rates is observed in H I-deficient galaxies (Kennicutt 1983; Gavazzi et al. 2002, 2006, 2013). The reduction in star formation tends to preferentially occur from the outside inward, resulting in truncated star-forming disks (e.g., Koopmann & Kenney 2004a, 2004b; Koopmann et al. 2006; Rose et al. 2010; Cortese et al. 2012; Fossati et al. 2013; Gullieuszik et al. 2017; Finn et al. 2018). If all of the gas content of a galaxy is removed, it will be fully quenched. One probable candidate for

the cause of the H I deficiency is ram pressure stripping (Gunn & Gott 1972), perhaps in combination with viscous stripping (Nulsen 1982) and thermal evaporation (Cowie & Songaila 1977). As a disk galaxy passes through a cluster on its orbit, its disk gas is subjected to ram pressure as it pushes through the hot intracluster medium (ICM) within the cluster. This pressure preferentially strips away disk gas from the outer disk, where it is more easily unbound, creating the outside-in H I gas disk truncation that is observed (e.g., Warmels 1988; Cayatte et al. 1990; Bravo-Alfaro et al. 2000, 2001; Chung et al. 2009; Scott et al. 2010). Although other nonhydrodynamical environmental mechanisms (e.g., gravitational tides; Valluri & Jog 1990, 1991; Moore et al. 1996, 1999; Gnedin 2003; Smith et al. 2015) can potentially strip gas from the outer disks of galaxies, hydrodynamical stripping mechanisms can strip the disk gas deep inside the optical disk of the galaxy, while leaving the stellar disk dynamically undisturbed (Vollmer et al. 2001, 2004; Vollmer 2003; except in gas-rich galaxies, where the removal of the gas potential may perturb the stellar disk—see Smith et al. 2013).

In nearby clusters, it is possible to catch the gas stripping process in action. Some gas-deficient spirals present prominent long one-sided H I tails that emanate from truncated gas disks and are spatially resolved in 21 cm maps thanks to their proximity (e.g., Oosterloo & van Gorkom 2005; Chung et al.

2009; Ramatsoku et al. 2019; Deb et al. 2020). In some cases, extragalactic star formation is observed to occur within the stripped gas streams (e.g., Owen et al. 2006; Cortese et al. 2007; Sun et al. 2007; Yoshida et al. 2008; Hester 2010; Smith et al. 2010; Fumagalli et al. 2011; Owers et al. 2012; Ebeling et al. 2014; McPartland et al. 2016; Poggianti et al. 2016; George et al. 2018; Grishin et al. 2021). Such galaxies tend to have a moderately enhanced star formation rate in their disks as well (e.g., Vulcani et al. 2018a; Roberts & Parker 2020; Vulcani et al. 2020). The presence of external star formation originally earned such galaxies the title of "Jellyfish" (JF) galaxies, as the streams of luminous young stars gave the impression of JF tentacles. But, more recently, the term JF galaxy has been used less strictly, to describe any galaxy with long one-sided streams of stripped material, whether it is starforming or not, and in this study we follow this latter naming convention.

Recently, there has been a boom in interest in JF galaxies (for a recent review, see Boselli et al. 2022). The streams of ram pressure stripped gas or extragalactic star formation have been revealed and studied using multiple different tracers in nearby clusters and groups. Each tracer provides a different window on the gas properties within the JF tails. H_α imaging relates to ionized gas at temperatures of roughly 10^4 K (Yagi et al. 2017; Fossati et al. 2018; Gavazzi et al. 2018). The VESTIGE survey (Boselli et al. 2018), which is a deep blind H_α survey in the Virgo cluster, is a good recent example of this. Integral field unit observations by the "GAs Stripping Phenomena in galaxies with MUSE" survey (GASP; Poggianti et al. 2017) have produced numerous detailed views of the ionized gas and star formation in JF galaxy tails (e.g., Gullieuszik et al. 2017; Vulcani et al. 2018b; Poggianti et al. 2019; Bellhouse et al. 2021). In star-forming galaxies, radio-continuum observations are sensitive to synchotron radiation from cosmic rays accelerated by supernovae. While undergoing ram pressure, tails of synchotron emission may be observed as the cosmic rays are stripped from the galaxy disk (Botteon et al. 2020; Chen et al. 2020; Lal 2020; Roberts et al. 2021a, 2021b, 2022). 21 cm observations can trace out the neutral atomic gas in JF tails (Minchin et al. 2019; Deb et al. 2020; Healy et al. 2021; Loni et al. 2021; Wang et al. 2021). Meanwhile, X-ray observations can trace out very hot ionized gas in JF tails (Boselli et al. 2016; Wood et al. 2017; Poggianti et al. 2019; Ge et al. 2019; Campitiello et al. 2021; Sun et al. 2021). Some JF galaxies were observed with multiple high-resolution observations (such as optical imaging with the Hubble Space Telescope and submillimeter observations with the Atacama Large Millimeter/submillimeter Array), which has enabled a detailed study of the gas properties in their tails (Abramson et al. 2016; Jáchym et al. 2017; Cramer et al. 2019, 2021).

Many JF galaxies often appear to be undergoing a dramatic transformation, some with ionized gas tails extending nearly 100 kpc in length (e.g., Smith et al. 2010; Yagi et al. 2010; Bellhouse et al. 2019). But we lack a clear understanding of the conditions in which the tails can form and survive. Even in the simplified case of a fixed ram pressure, we can expect that lower-density gas would be more rapidly accelerated from the disk, followed later by more dense gas (Tonnesen & Bryan 2009), meaning that the tails may appear differently, depending on the observational tracer that is used. Furthermore, the physics within the streams of stripped material is complex,

and poorly understood. The tail gas finds itself bathed in the hot ICM, and a combination of turbulence, magnetic fields, and feedback from newly formed stars can alter the tail gas properties and eventually mix out the tail gas into the ICM (Vollmer et al. 2001; Tonnesen & Stone 2014; Vijayaraghavan & Sarazin 2017; Müller et al. 2020; Sun et al. 2021; Gronke et al. 2022). The amount of material that is stripped evolves with the changing ram pressure, and the gas in the tails can have a wide range of densities and velocities.

The complexity of the physics involved means that it is difficult to model the tails accurately or predict the conditions under which JF tails will first become visible, as well as how long they will remain visible for. But a better understanding of this could potentially provide valuable clues on the gas stripping and quenching processes that newly accreted galaxies are subjected to on entering dense environments. The distance at which the tails appear from the cluster center can show when ram pressure first becomes effective, and the quenching process begins. This may be initiated when galaxies first enter the cluster, or it may occur much later, if the galaxies are initially surrounded by inflowing streams of ambient gas that infall alongside them (Bahé et al. 2013). Some models predict that ram pressure stripping could begin as far out as ∼2–3 virial radii, due to accretion shocks (Zinger et al. 2018). For a tail to exist there must be some disk gas to strip; so if we see a tail, we also know that some disk gas remains inside the disk at that position in the orbit. For example, if galaxies are fully stripped of their gas on first infall, then their tails may disappear prior to pericenter passage.

To try to improve our understanding of these issues in a cosmological context, a number of studies have searched for JF galaxies in large-volume cosmological hydrodynamical simulations that contain cluster-mass objects within their volume (Bahé et al. 2013; Bahé & McCarthy 2015; Marasco et al. 2016; Jung et al. 2018; Lotz et al. 2019; Yun et al. 2019; Troncoso-Iribarren et al. 2020). However, it is uncertain if all of the important physics required to model the stripping process are included or treated sufficiently accurately. In many cases, massive clusters tend to overquench their satellites (Brown et al. 2017; Davé et al. 2017; Stevens et al. 2019; Donnari et al. 2021; Xie et al. 2020), perhaps as a result of insufficient resolution and/or an interaction between subgrid physics feedback implementations and the ram pressure stripping process (Bahé & McCarthy 2015; Emerick et al. 2016; Kazantzidis et al. 2017; Zoldan et al. 2017; De Lucia et al. 2019). Therefore, it is not clear if the conditions under which JF tails appear and how long they last for in these simulations can be assumed to directly match the observed objects.

As an alternative to self-consistent hydrodynamical cosmological simulations, some studies have had success in applying analytical models to observed ram pressure stripped galaxies and their tails (Jaffé et al. 2015, 2018; Gullieuszik et al. 2020). In this case, the strength of the ram pressure is estimated from a galaxy's location in a projected velocity–radius phase-space (PS) diagram, combined with an estimate for the ICM radial density distribution. There are already some uncertainties introduced, as projection effects may affect the galaxy's location in PS and, even if X-ray observations are available for the cluster of interest, they are normally only available near the cluster center and extrapolated out to larger clustocentric radii. The impact of this estimated ram pressure on the disk galaxy is then calculated using an analytical equation based on

a Gunn & Gott (1972) formalism, where the ram pressure is compared to the disk restoring force at different radii throughout the disk. As a result, there are many factors that can affect the stripping efficiency, including the shape and scale length of the radial disk density profile, how extended the gas disk is with respect to the stars (Cayatte et al. 1994), and the restoring force from a stellar bulge and the dark matter halo (Abadi et al. 1999), and it is challenging to know all of these properties for a large sample, especially given that we would really need to know them prior to the onset of stripping. The gas disk truncation radius is also calculated assuming face-on stripping, although hydrodynamical simulations show that this assumption is reasonable to first order, as long as the disk is not close to edge-on to the ram pressure wind (Vollmer et al. 2001; Roediger & Brüggen 2007).

Given the current limitations of cosmological hydrodynamical simulations, and the large number of parameters and uncertainties in the existing analytical models, in this study we seek to develop a novel approach that has fewer parameter dependencies. The aim is to try to better determine the conditions under which the tails of observed JF galaxies appear and when they disappear. This new approach combines two observational measurements: the distribution of JF tail angles measured with respect to their group/cluster center, and their observed locations in projected velocity–radius PS diagrams.

As larger samples of JF galaxies have been accumulated, the distributions of their tail directions have increasingly been used to interpret whether galaxies are on first infall into their hosts. This has been attempted observationally in H I (Chung et al. 2007), optical (Poggianti et al. 2016; Roberts & Parker 2020), Hα (Durret et al. 2021; Liu et al. 2021), UV (Smith et al. 2010), X-ray (Merrifield 1998) and radio continuum (Roberts et al. 2021b, 2021a). From these studies, the general conclusion is that the high fraction of objects with tails pointing away from their host centers implies that these objects are on their first infall into their host along quite radial orbits. Unlike the observations listed above, a much flatter tail angle distribution was measured in the hydrodynamical cosmological simulations of Yun et al. (2019).

Projected velocity–radius PS diagrams have also been shown to provide useful constraints on the time since the galaxies first fell into their hosts (Muzzin et al. 2014; Oman & Hudson 2016; Rhee et al. 2017; Pasquali et al. 2019). A number of authors have applied these diagrams to samples of JF galaxies (McPartland et al. 2016; Yoon et al. 2017; Jaffé et al. 2018; Roberts & Parker 2020; Liu et al. 2021; Roberts et al. 2021a, 2021b). Similar to the results based on tail directions, the general conclusion drawn is that JF galaxies tend to prefer the "recent-infaller" area of the PS diagram (see, for example, Figure 6 of Rhee et al. 2017).

However, this study represents the first attempt to simultaneously use the observed JF tail directions combined with their location in PS in a complementary manner to try to quantitatively constrain where their tails form and how long they last for. This is accomplished using cosmological simulation results and Bayesian parameter estimation. We apply our novel method to a sample of LOFAR radio-continuum JF galaxies in groups and clusters. The contents of our paper can be summarized as follows. Our observational sample is described in Section 2.1, and our cosmological simulations are described in Section 2.2. Our method is described in Section 3, and we test the method with mock

observational data sets in Section 4. The results of applying the method to the full JF sample are presented in Section 5.1, and to JF subsamples in Section 5.2. We summarize and conclude in Section 6. Throughout this study, we assume a Λ cold dark matter cosmology of $\Omega_m = 0.3$, $\Omega_\Lambda = 0.7$, $\Omega_b = 0.047$, and $h_0 = 0.7$.

2. Sample

2.1. LOFAR JFs in Group-/Cluster-mass Hosts

Our main observational sample is the sample of JF galaxies presented in Roberts et al. (2021a, 2021b; hereafter R21a/b). JF galaxies were visually identified by the presence of 144 Mhz radio-continuum tails in groups and clusters covered by the LOFAR Two-meter Sky Survey (LoTSS; Shimwell et al. 2017, 2019). Contamination by active galactic nuclei was found to be less than 5%–10% in the cluster sample of R21a. In star-forming galaxies, LoTSS is sensitive to synchrotron emission from cosmic rays accelerated by supernovae. For star-forming galaxies experiencing ram pressure stripping, tails of synchrotron emission may be observed as these cosmic rays are stripped from the galaxy disk. Thus, the visibility of the tails at 144 Mhz requires star formation in the disk, but not necessarily in the tails themselves. LoTSS combines a high resolution ($\sim 6''$) with high-sensitivity uniform coverage (~ 100 μJy beam^{-1}) over a large area, and will eventually cover the entire northern sky. The groups and clusters in R21a and R21b are selected from spectroscopic Sloan Digital Sky Survey (SDSS) group/cluster catalogs (Wang et al. 2014; Lim et al. 2017). For simplicity, we hereafter refer to these groups and clusters collectively as "hosts." Objects at a projected radius of < 1 R_{180} (where R_{180} is the radius containing a region with 180 times the critical density of the universe) and a line-of-sight velocity difference $< 3\sigma_{rms}$ (where σ_{rms} is the velocity dispersion of the host) were considered to be associated with the hosts. All objects have optical counterparts. Galaxy star formation rates and stellar masses were taken from the GSWLC-2 catalog (Salim et al. 2016, 2018) and measured based on spectral energy distribution fitting with CIGALE (Boquien et al. 2019). Only galaxies with a specific star formation rate sSFR $> 10^{-11}$ yr^{-1} (i.e., star-forming) were included in the sample. Due to the decreasing sensitivity of LoTSS to low-mass star-forming galaxies (R21a), we also remove galaxies with masses below $10^{9.5}$ $M_\odot$. This suppresses a tendency for us to detect galaxies with lower masses than this limit only for low redshifts, which would otherwise make comparison with the simulations challenging.

JF galaxies displaying long tails are expected to be quite asymmetrical in shape. Therefore, we also consider a shape asymmetry parameter, defined as

$$A_s = \frac{\Sigma |X_0 - X_{180}|}{2 \times \Sigma |X_0|}, \tag{1}$$

where X_0 and X_{180} are the complete radio-continuum map of an object and its 180° rotation, respectively (Pawlik et al. 2016). We only consider objects with $A_s > 0.3$, which reduces the number of galaxies that we must visually inspect by filtering out symmetrical objects. R21a states that this choice of threshold includes $\sim 85\%$ of the visually identified LoTSS JF galaxies in clusters, while excluding $\sim 70\%$ of the LoTSS sources in clusters that are not identified as JFs.
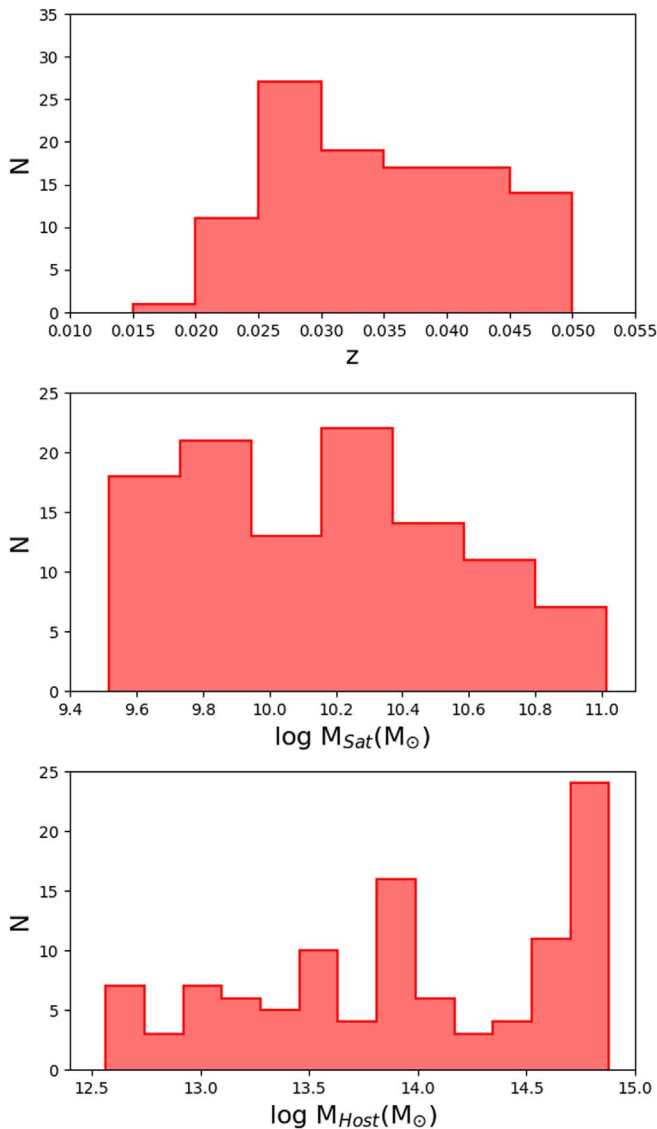
Figure 1. The general properties of the main LOFAR JF sample. Top: redshift distribution. Center: distribution of stellar masses of satellite galaxies. Bottom: distribution of host masses.

We measure the noise levels in the background surroundings of each individual galaxy, and find values that range from 40 to 280 μJy beam^{-1}. To reduce the impact of varying noise levels on our results, we take a cut for galaxies with noise levels greater than 200 μJy beam^{-1}, which are likely associated with artifacts or bright contaminating sources. The final sample of JFs contains 106 galaxies in 68 hosts. We also test a more conservative 150 μJy beam^{-1} noise cut, but find that this reduces our number statistics to only 89 galaxies, and the results do not change significantly (see Figure 11 in Appendix A).

Histograms of the redshift, stellar mass, and host mass distribution of our main sample can be found in Figure 1. The galaxies have stellar masses in the range $10^{9.5}$–$10^{11} M_\odot$, and their hosts range in mass from low-mass hosts ($10^{12.5}$–$10^{13} M_\odot$) to massive clusters ($10^{14.5}$–$10^{15} M_\odot$). According to R21b, the observed fraction of JFs is higher in more massive hosts. The redshift range is from $z = 0.015$ to 0.05. The lower limit is because the SDSS group catalogs contain few galaxies with $z < 0.01$. The imposed upper limit is a little arbitrary, but with

increasing redshift it becomes increasingly difficult to detect low–surface brightness tails, and short tails become more difficult to resolve. Some examples of JF galaxies (radio-continuum contours overlaid on optical imaging) from our sample can be seen in Figure 2. For similar images of the full sample, see the Appendices in R21a and R21b.

2.2. N-body Cosmological Simulations

To model the observations, we use an *N*-body cosmological simulation that was run as a dark matter–only model using the GADGET-3 code (Springel et al. 2001). To generate the initial conditions at redshift = 200, the Multi Scale Initial Condition software (MUSIC; Hahn & Abel 2011) was used. The CAMB package (Code Anisotropies in the Microwave Background; Lewis et al. 2000) was used to calculate the linear power spectrum. We analyze a single cosmological volume with dimensions $120 \times 120 \times 120$ Mpc h^{-1}. The dark matter particles have a fixed mass of $1.072 \times 10^9 M_\odot h^{-1}$ in all the simulations. Output files were produced at ~100 Myr intervals, consisting of the mass, velocities, and positions of dark matter particles for each snapshot, down to redshift zero.

We then run the ROCKSTAR halo finder on the dark matter particle files to build a catalog of halos at each snapshot (Behroozi et al. 2013). In ROCKSTAR, halos are identified using a hierarchical friends-of-friends approach that combines 6D PS information and 1D time, and provides information on the merging history as well. We remove all halos with a mass lower than $10^{11} M_\odot$ in order to ensure that our halos are well resolved (more than 100 particles per halo). The merger tree is built with CONSISTENT TREES (Behroozi et al. 2013), which combines particle IDs with halo trajectory information to improve the linking of halos between snapshots. In total, there are 692 host halos (central halos with a mass greater than $10^{13} M_\odot$) in our simulation volume, and we record 22,813 first-infaller halos that fall into these hosts.

3. Method

3.1. Painting Tails onto First-infaller Satellite Halos in Dark Matter–only Cosmological Simulations

Using the cosmological simulations described in Section 2.2, we produce simulated projected tail angle histograms and simulated locations in projected PS for comparison with the observations. As our cosmological simulations are dark matter only, there are no genuine hydrodynamical gas tails within them. Therefore, our approach is to "paint on" the tails. We add them on and remove them, according to different assumptions in our model about their visibility. The three main parameters that we consider in the model are listed below (see also Figure 3).

*r*1. For an object on first infall into the host, the JF tail is assumed to first become visible at the 3D radius *r*1, which is given as a percentage of the host's r_{200} (the radius containing a volume with 200 times the critical density of the universe), and allowed to vary from 10% to 200% in steps of 1%. For example, 200% means that the JF tails appear when the galaxy is infalling for the first time and passes the 3D radius of 2 r_{200} from the host center. In Jaffé et al. (2018), optical JF candidates were seen out to projected radii of close to 2 r_{200}, and so we provide a similar extended range of *r*1 to allow a wide parameter space to be explored. We note that although the LOFAR sample is limited to remain inside a projected radius of
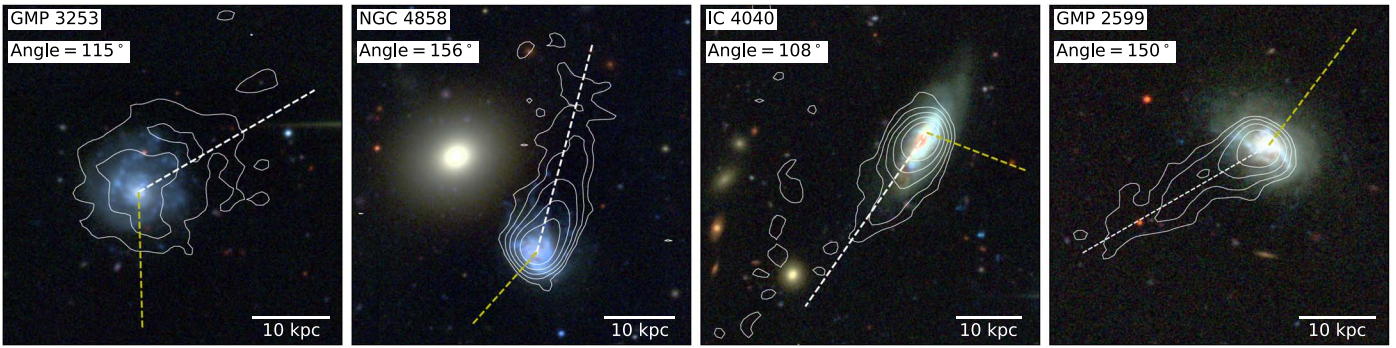
Figure 2. Example images of four Coma cluster galaxies from R21a. Similar images of all of the galaxies in our sample can be seen in the Appendices in R21a and R21b. The background RGB images consist of the *i*, *g*, and *u* bands from the Canada France Hawaii Telescope, and the contours are the LOFAR 144 MHz continuum. The lines indicate the measured tail directions (white dashed) and the direction to their host's center (yellow dashed), while the angle between them is shown beneath the galaxy title in the upper left corner.

R_{180} (for comparison, R_{180} is typically 5% larger than r_{200}; Reiprich et al. 2013), we can still model those galaxies with 3D radii out to $2\,r_{200}$. Thanks to projection effects, some of these objects will fall inside the limiting projected radius and can be considered in the modeling. Therefore, to account for this, we simply use a projected radius limit on the simulations that matches the observations.

δ. In the simplest scenario, we assume that the tail direction points back in the opposite direction to the motion of the halo, with respect to the host's frame of reference. However, it is known from hydrodynamical simulations that the gas being stripped from a galaxy does not respond instantly to ram pressure and takes a finite time to be accelerated (Roediger & Brüggen 2007). Similarly, when galaxies rapidly change their orbital direction (for example, near pericenter), a finite time will be required for the tail to change direction, which is expected to be of the order of the time to form a new tail by traveling from the disk out to the end of the tail. Therefore, we introduce the delay parameter δ, which is the delay (in Myr) of the response of the tail direction to a change in orbital direction. We allow δ to vary from 0 to 500 Myr in 100 Myr time steps. For example, $\delta = 0$ Myr corresponds to the tail direction pointing directly opposite to the orbital motion of the halo, with respect to the host measured at that instant, meaning that there is no delay. Meanwhile, if $\delta = 200$ Myr, the tail direction points opposite to the orbital motion measured 200 Myr earlier, meaning that the change in tail direction has been delayed by 200 Myr. The 500 Myr upper limit of δ was estimated from hydrodynamical wind-tunnel simulations (Tonnesen 2019), based on the time required to form a new gas tail of similar length to those observed (tens of kilometers). We also repeated our tests using a more extreme 1 Gyr upper limit for δ, but our results were very similar and did not alter our main conclusions.

$t2$. Finally, we record the moment when the halo passes the pericenter (the minimum 3D distance from the host center along the halo's orbit), and then assume that the tail remains visible for a chosen length of time ($t2$) in Myr after the moment of pericenter. $t2$ varies from −400 to +2000 Myr, in 100 Myr time steps. The negative value of the lower limit corresponds to the tail disappearing from view as early as 400 Myr before pericenter, while positive values correspond to tails disappearing after pericenter. As with $r1$, we choose a generous range of $t2$ to allow a wide area of parameter space to be explored.

By "painting on" the tails in this manner, we are able to quickly and efficiently cover a large area of parameter space,
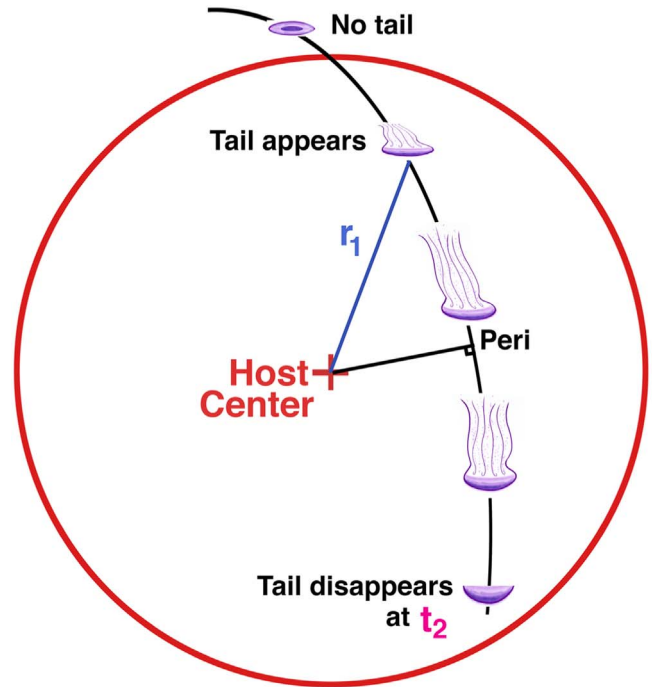
r_1 = radius when Tail appears [% of the host r_{200}]

δ = delay of Tail direction change [Myr]

t_2 = time since Peri when Tail disappears [Myr]

Figure 3. Cartoon schematic illustrating the key parameters of the model. For satellite halos on first infall into the host halo, the tails first appear at a specified distance $r1$ from the host center, provided as a percentage of the host halo's r_{200} (indicated by the red circle). The tails generally point in the opposite direction to the orbital trajectory of the satellite halo through the host halo, as shown in the schematic, but the delay parameter δ (in Myr) allows the tail direction to have a delayed response if the orbital trajectory changes direction rapidly. The tails shown in the schematic point exactly opposite to the orbital trajectory line, meaning $\delta = 0$ Myr. Finally, the tail disappears from view a specified time $t2$ (in Myr) after the pericenter occurs, where $t2$ can be negative if the tail disappears before pericenter.

varying all three parameters in the steps described above to form a 3D grid of the models, where each grid point represents a unique combination of $r1$, δ, and $t2$ values. In principle, we could paint the tails onto the simulated halos at a chosen instant (e.g., $z = 0$), to mimic the redshift of the observed galaxies.
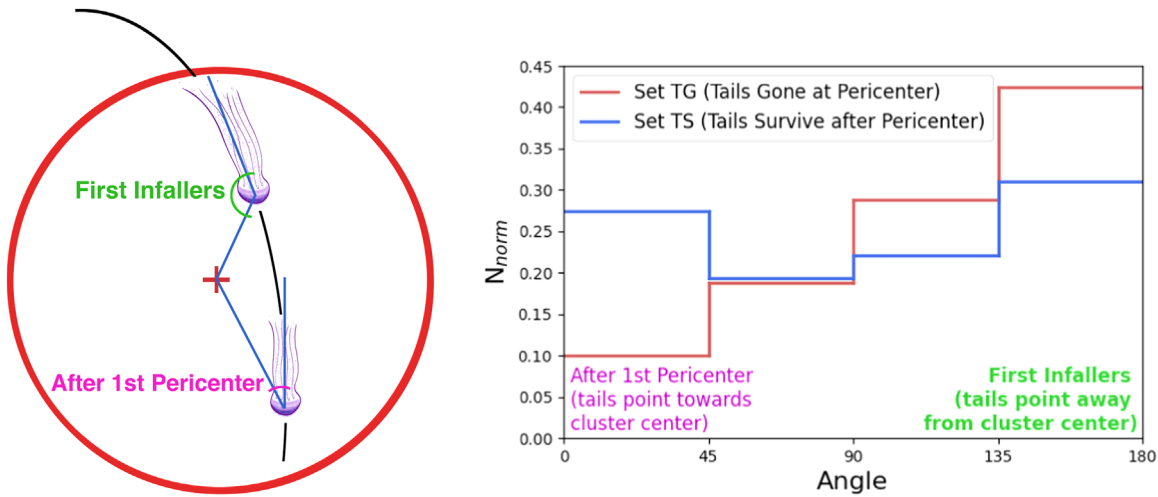
Figure 4. Left: cartoon illustrating how the 3D angle of the JF galaxy tail (measured with respect to the host's center) depends on whether the galaxy is on first infall (the large angle shown with the green arc) or has passed orbital pericenter (the small angle shown with the pink arc). The red circle illustrates the cluster r_{200}. Right: for illustrative purposes, we present the projected tail angle histograms of two sets of model galaxies. In the first set (red histogram, labeled "Set TG"), the galaxies lose their tails at the instant that they reach pericenter ($r1$, δ, $t2 = 100, 500, 0$). The second set (blue histogram, labeled "Set TS") is identical, except that they maintain their tails for 500 Myr after pericenter ($r1$, δ, $t2 = 100, 500, 500$). The red histogram illustrates that projection effects alone can allow some galaxies to fall into the lowest angle bin ($0°–45°$), but an increase in the object numbers in this bin (as we will later show is found in our observed sample; see the top panel of Figure 8) requires galaxies to maintain their tails after pericenter passage.

However, in practice, we find that the measured tail angle distributions change very little over the last several Gigayears, because the orbits of the halo population do not change significantly on such short timescales. Therefore, we can stack the results over the last two Gigayears (20 snapshots), which greatly increases our statistics without altering the shape of the tail angle distributions. As a result of this and the large numbers of simulated hosts and first-infaller satellites, there are excellent statistics contained within almost every 3D grid point of the model in $r1$, δ, and $t2$ space. 98% of the grid points contain samples of more than 1000 tails. Only 0.02% of the grid points contain samples of fewer than 106 tails (the size of the observed sample). For each set of parameters (e.g., $r1$, δ, $t2$), the tails are painted on in 3D, and we then project them down a single line of sight to produce their projected (2D) tail angle distributions, to match the projected observed tail direction histograms. As a result of good statistics in the number of hosts and first-infaller satellites, we find negligible changes in the histograms for different line-of-sight choices. We also see little evidence for a clear change in the shape of the histograms if we split the infalling halos by mass. Similarly, we also take their 3D velocities and radii within the host halos and project them into a projected (2D) PS diagram (line-of-sight velocity versus projected radius from the host halo center), and count relative numbers in each region of PS, as we do for the observed JFs, as described in Section 3.3.

3.2. Projected Tail Directions

For each observed JF galaxy, we visually estimate the projected angle of the tail with respect to the host's center, as described in R21a and R21b. A tail pointing directly toward the host's center is defined as having a tail angle of $0°$ and a tail pointing directly away from the host center has a tail angle of $180°$. We build up a histogram of the tail angles, using $45°$ wide angle bins. As the angle bins are chosen to be quite wide, the overall shapes of our histograms are not sensitive to small inaccuracies in the measurement of the tail angles.

The left panel of Figure 4 presents a schematic of how the direction of a ram pressure stripped tail depends on whether it is before or after pericenter in its orbit. Objects on first infall will have high tail angles in 3D, as their tails point away from the host's center in 3D. After pericenter, objects that still have tails will have low tail angles in 3D, as their tails point toward the host's center.

However, the observed tail angles are seen in projection, not in 3D. To see how the projected tail angle histograms depend on whether galaxies keep their tails past pericenter, we compare for illustrative purposes two model data sets in the right panel of Figure 4. The model parameters are ($r1$, δ, $t2$) = (100, 500, 0) and (100, 500, 500) for the red and blue histograms, respectively. In the first set (red line, labeled "Set TG"), the tails disappear at the moment of pericenter, and so in 3D all the tails point away from the host's center. But thanks to projection effects, some objects can still have projected tail angles of $<90°$, although the shape of the histogram always slopes down toward the lower projected angles (see the overall shape of the red histogram). In the second set (blue line, labeled "Set TS"), the tails remain visible for 500 Myr after pericenter. Only if the tails survive past pericenter can the $0°–45°$ bar actually be higher than the $45°–90°$ bar (as shown by the blue histogram). This is important, as we will see in Section 5.1 that the main LOFAR JF sample also presents this feature.

3.3. Locations in Projected PS

Besides the tail angle distributions, we can also use the locations of the JF galaxies in a projected velocity–radius PS diagram as an additional observational constraint. To do so, we count the relative number of JF galaxies in four regions in PS. The JF galaxies are separated at $r/r_{200} = 0.5$ and $V/\sigma = 1.0$, as shown in the left panel of Figure 5. The choice of two bins in projected distance and two bins in line-of-sight velocity means that the existence of both a radial gradient and a velocity gradient can potentially influence the results.

The right panel of Figure 5 shows how the shape of the corresponding projected tail angle histogram is sensitive to the
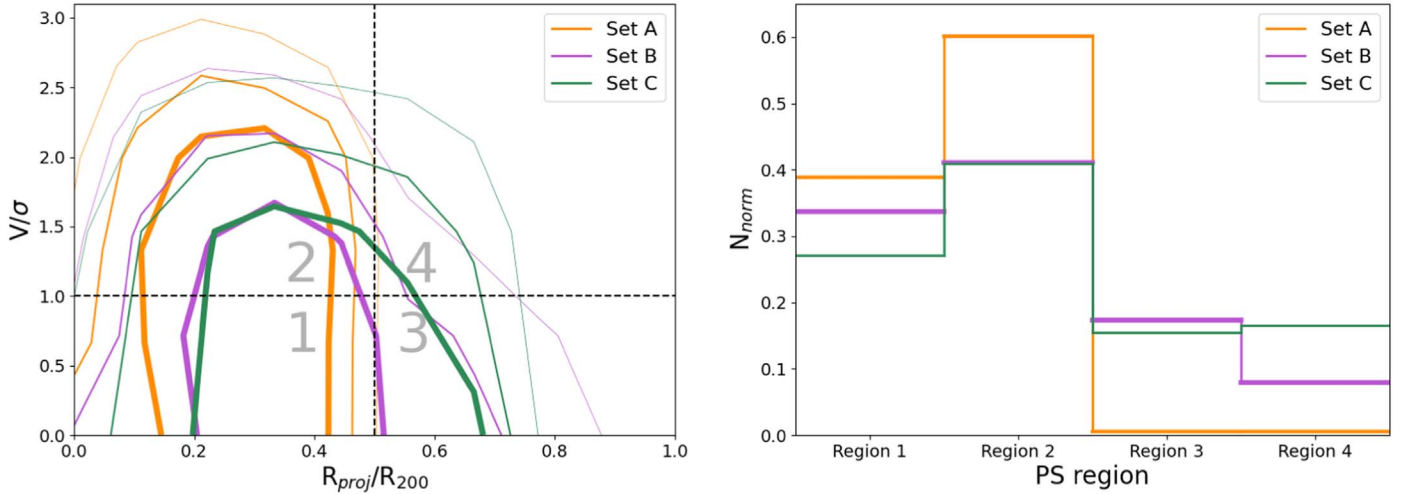
Figure 5. The left panel illustrates the four regions in PS that we consider (labeled "1–4"). For illustrative purposes, we consider three sets of model galaxies. The model parameters of Sets A, B, and C are $(r1, \delta, t2) = (50, 500, 0)$, $(50, 500, 1000)$, and $(75, 500, 0)$, for orange, purple, and green, respectively. Set A and Set B are identical, except the tails last for 1000 Myr after pericenter in Set A, while they disappear at pericenter in Set B. Set B and Set C are identical, except the tails first become visible at 50% of the host's r_{200} in Set B compared to 75% for Set C. The thick, medium, and thin contours in the left panel contain 25%, 50%, and 75% of each Set, respectively, while the right panel shows their histograms. See the text for further details of the three model data sets.

Table 1
Adopted Priors

Parameter	Prior Type
r_1/r_{200}	Uniform over (10, 200) in %
δ	Uniform over (0, 500) in Myr
t_2	Uniform over (−400, 2000) in Myr

cluster radius at which the tails first appear, and/or how long they last for after pericenter. For illustrative purposes, we compare three model data sets (Sets A, B, and C). The model parameters of Sets A, B, and C are $(r1, \delta, t2) = (50, 500, 0)$, $(50, 500, 1000)$, and $(75, 500, 0)$, for orange, purple, and green, respectively. Set A (orange) versus Set C (green) illustrates the change if the clustocentric radius when the tails first appear is varied from 50% to 75% of the host's r_{200}, respectively, while keeping the other parameters fixed. If the radius in which the tails appear is larger (Set C), more JFs appear at larger projected radii, as expected (Set C has more galaxies in regions 3 and 4 than Set A). Set A (orange) versus Set B (purple) illustrates the change if the duration that the tails are visible for after pericenter is varied from 0 to 1000 Myr, while keeping the other parameters fixed. If the tails can last a long time after pericenter (Set B), more objects appear at larger radii, because they move out to these radii after passing pericenter (Set B has more galaxies in regions 3 and 4, especially in region 3). As a result, by comparing the sets, we can see how varying both the radius at which the tails first appear and how long they last for after pericenter alters the distribution of the galaxies within the PS regions (see the right panel of Figure 5). As a result, estimates of where the JF tails appear and how long they remain visible for are much more constrained if we also consider their distributions in PS alongside the tail angle measurements. This combination of measurements allows us to better separate first-infallers from objects that have passed pericenter. We will directly demonstrate the individual roles of the PS and tail angle measurements for constraining the model in Section 4.

3.4. Bayesian Parameter Estimation

In order to estimate the three model parameters (r_1, δ, and t_2), we adopt the Bayesian approach and sample the posterior using the Markov Chain Monte Carlo (MCMC) method (see Sharma 2017). Assuming that the observational data are from normal distributions, we set the likelihood as below:

$$\ln L = -\frac{1}{2}\sum_i \frac{(\mathrm{obs}_i - \mathrm{model}_i)^2}{\mathrm{obserr}_i^2}, \qquad (2)$$

where obserr_i is provided by bootstrapping. As there are four angle bins and four PS region bins, the tail angles and PS locations have equal weight when matching the model to the observations.

As presented in Table 1, we use uniform priors for all three model parameters over the modeled parameter range, as we do not have a clear reason to give preference to any particular values, at least within the specified ranges. These priors guarantee the posterior propriety emphasized in Tak et al. (2018); that is, the resulting posterior is a probability distribution.

To sample the posterior, which is proportional to the product of the likelihood and prior, we employ the affine-invariant ensemble sampler called emcee (Foreman-Mackey et al. 2013, 2019). We sample the posterior as in Shinn (2020), monitoring the convergence of the MCMC sampling with the integrated autocorrelation time (τ_{int}), which is defined as below:

$$\tau_{\mathrm{int}} = \sum_{t=-\infty}^{\infty} \rho_{xx}(t), \text{ where } \rho_{xx}(t) = \frac{\mathbb{E}[(x_i - \bar{x})(x_{i+t} - \bar{x})]}{\mathbb{E}[(x_i - \bar{x})^2]}. \qquad (3)$$

Here, ρ_{xx} is the autocorrelation function for the sample sequence $\{x_i\}$, t is the time difference—or distance—between two points in the sequence $\{x_i\}$, $\bar{x}$ is the mean of sequence $\{x_i\}$, and $\mathbb{E}[\cdot]$ means the expectation value.

When the τ_{int} values of all three parameters are low enough at the final iteration to have an effective sample size (ESS) of >2000, we stop the sampling (see Shinn 2020 for the details).
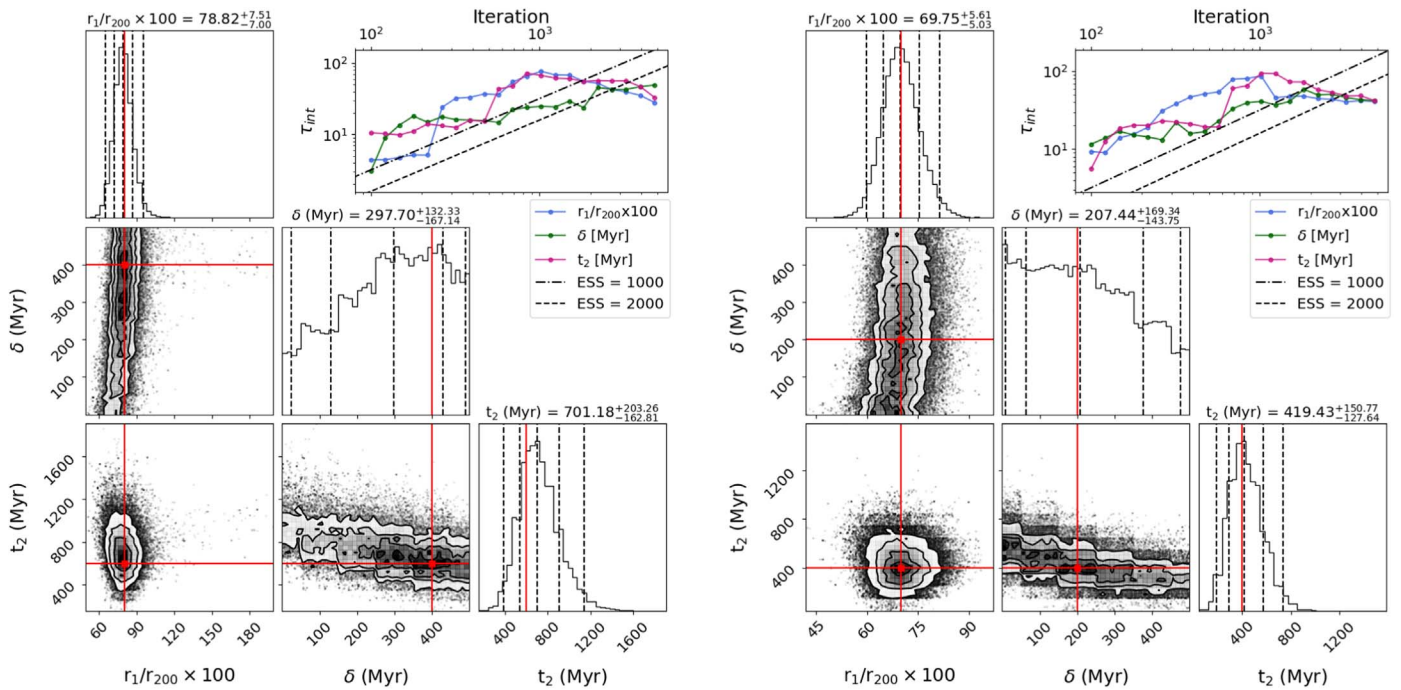
Figure 6. Results of the MCMC sampling for Mock 1 (left) and Mock 2 (right). For each mock test, the panels are arranged as follows. In the upper right, a convergence monitoring panel is shown for each parameter (see the legend). The other panels take the form of corner plots. The panels with grayscale shading and contours are 2D PDFs comparing two different model parameters. The upper left, center, and lower right panels are marginalized PDFs of r_1/r_{200}, δ, and t_2, respectively. In the marginalized PDF panels, the central vertical dashed line is the median of the distribution, while the surrounding vertical dashed lines show the 68% and 95% credible intervals. The subtitles of the panels provide the median values, and the errors are for the 68% credible interval. The red line shows the input value for that parameter. Our method is successful at reliably constraining the input values used to make both the mocks—for all the parameters, the input value falls within the 68% credible interval around the median of the marginalized PDFs.

This condition means that we have >2000 independent samples for the probability density distributions of the three parameters. We note that abrupt, long-lasting increases of τ_{int}, which cause the abrupt ESS decreases (worsening the convergence), were also observed during the sampling, as reported in Shinn (2020); hence, we emphasize that convergence monitoring is important during the MCMC sampling.

Although in the model we paint JF tails onto all the first-infaller halos, we note that the comparison between the observed and simulated galaxies is done with normalized histograms. This means that we are not necessarily assuming that all galaxies infalling into massive hosts form tails. Rather, we assume that the observed galaxies exist in a randomly chosen subsample of the first-infaller halos in the cosmological simulation.

4. Testing the Method with Mocks

In order to test the approach we use when comparing the observations with the models, we create two mock observational data sets. These are selected from the model grid. Mock 1 and Mock 2 have $(r_1, \delta, t_2) = (80, 400, 600)$ and $(70, 200, 400)$, respectively. We will later see in Section 5.1 that these choices of mock fall in a similar area of parameter space as the median results of our observed JF sample. From the model, we directly have normalized histograms of the angle bins and PS regions, and we additionally give each data point an error bar of similar size to those of the observational sample (in this case, we assume a fixed error of 0.05 on each normalized histogram bar).

The left and right columns in Figure 6 show the results for Mock 1 and Mock 2, respectively. The upper left, central, and

lower right panels of each column are the marginalized probability density functions (PDFs) of r_1/r_{200}, δ, and t_2. The red lines show the values of the input parameters (r_1, δ, t_2) for each mock. In both mocks, the PDFs of r_1/r_{200} (upper left) and t_2 (lower right) are well behaved, in that they show a clear single peak. The central dashed vertical line is the median of the PDF. The other two vertical dashed lines encompass 68% and 95% of the distribution on either side of the median. For r_1/r_{200} and t_2, it is clear that the model's input value is located within the 68% credible interval for all the parameters and in both Mock 1 and Mock 2. Indeed, generally it is difficult to distinguish the median lines from the r_1/r_{200} and t_2 input values, with the single exception of the Mock 1 t_2 PDF. This indicates that the method provides good constraints on these two parameters. Similarly, this shows that these parameters are both influential for deciding the shape of the projected tail angle histogram and the projected PS region histogram.

However, in both mocks, the PDF of the delay parameter δ is not so well behaved. Neither show a well-defined peak, and instead we see a sloping distribution across the full parameter range, with a preference for high values of δ in Mock 1 and low values in Mock 2. Despite this, the input value still falls within the 68% credible interval. Although the relative uncertainty (defined as the width of the 68% credible interval divided by the median value) is large compared to the other parameters, because of the shape of the PDF (e.g., the relative uncertainties for r_1/r_{200}, δ, and t_2 are 0.18, 1.0, 0.52 for Mock 1 and 0.15, 1.50, 0.66 for Mock 2). This means that the median δ value is more poorly constrained, which likely indicates that the delay parameter is a less important parameter for controlling the shapes of the angle bins and PS region histograms, at least for the tested region of parameter space.
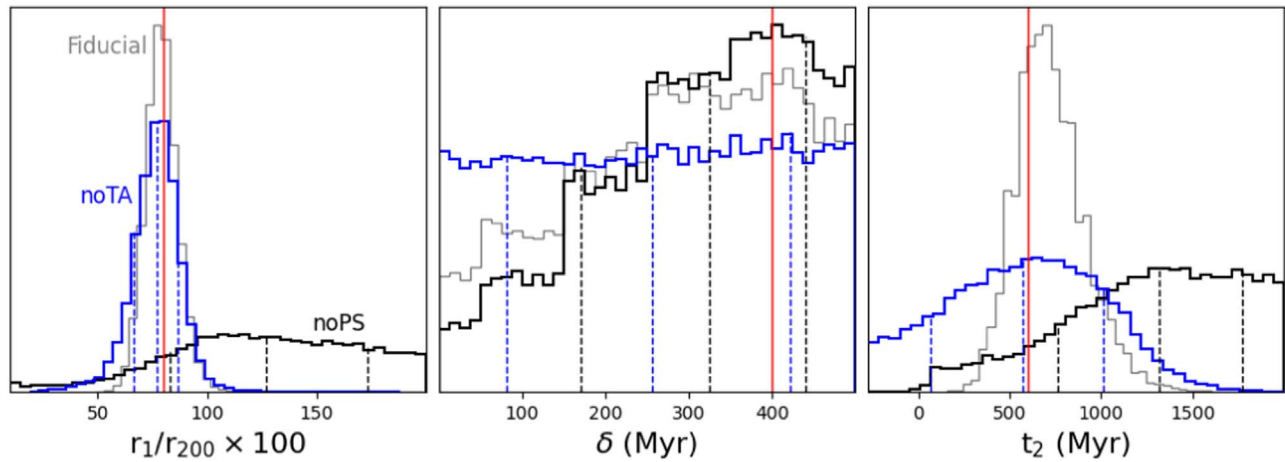
Figure 7. The results of the MCMC sampling for Mock 1. The red vertical line shows the input values of Mock 1. The gray histograms show the case when both tail angles and PS constraints are applied (labeled "Fiducial"; identical to the results in Figure 6). The black histograms are the same as the Fiducial case, but when the constraints from the PS are neglected (labeled "noPS"), and the blue histograms are when the constraints from the tail angles are neglected (labeled "noTA"). The vertical dashed lines show the median and the 68% credible interval (the median is the central dashed line) of each histogram. Without PS constraints, the Mock 1 input value fails to fall within the 68% credible limit of the "noPS" PDF for both $r1/r_{200}$ and $t2$. Without tail angle constraints, the $t2$ distribution is much wider, meaning that it is more poorly constrained.

To understand the importance of considering the locations of JF galaxies in projected PS in addition to their projected tail angles, we repeat the Mock 1 test, but using only the projected tail angles to constrain the model. The impact that this has on the marginalized PDFs of the three parameters can be seen in Figure 7. The black histograms are the no-PS results (labeled "noPS"), for comparison with the gray histograms (labeled "Fiducial") that are constrained by both tail angles and PS results. The PDFs of $r1/r_{200}$ and $t2$ become much broader and have a less clearly defined main peak, as well as long tails toward higher values. As a result, for both of these parameters, the median value (the central dashed vertical line) is no longer within 1σ of the input value (the red vertical line). However, there is a less significant change to the δ parameter PDF, which already had a broad distribution, even when applying the PS constraints.

We also consider the case where we use only the PS results, and neglect the tail angles, when constraining the model (the blue histograms; labeled "noTA"). In the first panel, the similarity between the gray and blue histograms shows that the tail angle measurements provide little constraint on the $r1/r_{200}$ values. This is because most first-infallers have quite plunging radial orbits, so the tail angle distributions should be quite similar until the galaxies approach and pass pericenter. Nevertheless, the 68% credible interval of the blue histogram is slightly wider than the gray one in the left panel (38% wider), meaning that $r1/r_{200}$ is slightly better constrained with tail angle measurements. In the central panel, we see that the δ parameter distribution is flatter, and the credible interval is slightly wider than in the "Fiducial" case. In the right panel, we see that the $t2$ parameter distribution is considerably wider for the "noTA" model compared to the "Fiducial" case (the 68% credible interval is a factor of 2.6 times wider, although the median is actually even closer to the input value). This highlights the importance of the tail angle measurements for constraining the $t2$ parameter. Finally, comparing all three histograms, we see that, for Mock 1, the $r1/r_{200}$ results rely strongly on information about the galaxy locations in PS, while the $t2$ results rely strongly on both tail angle information and locations in PS.

In summary, our mock tests demonstrate that, with the combination of both angle bin and PS region histograms, our

approach can provide useful constraints on the values of $r1/r_{200}$ and $t2$. But it is difficult to tightly constrain the δ parameter in this manner, as the model is less sensitive to changes in δ. With this in mind, we now attempt to apply our new methodology to the observed data set.

5. Results and Discussion

5.1. Results from the Main LOFAR JF Sample

In this section, we begin by applying our methodology to the complete LOFAR JF galaxy sample, which consists of 106 galaxies shared across 68 hosts. We then split the main sample into separate subsamples in the next section. In Figure 8, we present normalized histograms of the angle bin (top panel) and PS regions (bottom panel). The tail angle measurements are the same as those made in R21a and R21b, and are defined with respect to the stellar mass–weighted host center. In principle, X-ray centers might provide better measurements of the potential minimum within a host, but consistent X-ray center measurements are not available for all of our hosts. Uncertainties (shown as the error bars on the histogram bars) are calculated by bootstrapping 100,000 times.

We note that tail angle histogram (top panel) is peaked at high tail angles (the $135°–180°$ bar) and low angle bins (the $0°–45°$ bar), with the minimum in the $45°–90°$ bar. As noted in Section 3, this feature already highlights that a significant fraction of the objects in the observed sample must maintain their tails for some time after pericenter passage. Meanwhile, in the PS region histogram, we see that most galaxies are found in region 1 and region 2 (the two regions on the left, at a projected radius of $r < 0.5r_{200}$; see Figure 5).

These histograms and their uncertainties are now used as an input to our method. The results are shown in Figure 9. Similar to the mock tests in Section 4, the marginalized PDFs of $r1/r_{200}$ (the upper left panel) and $t2$ (the lower right panel) show a well-defined single peak, while the δ parameter shows no clear peak and is less well constrained. The median value of $r1$ is $(76.0^{+4.2}_{-4.1})\%$ of r_{200}, and $t2$ is $(479.4^{+115.4}_{-106.8})$ Myr, while the median δ value is $(314.6^{+129.8}_{-180.9})$ Myr. Here, the upper and lower limits encompass the 68% credible interval. The relative
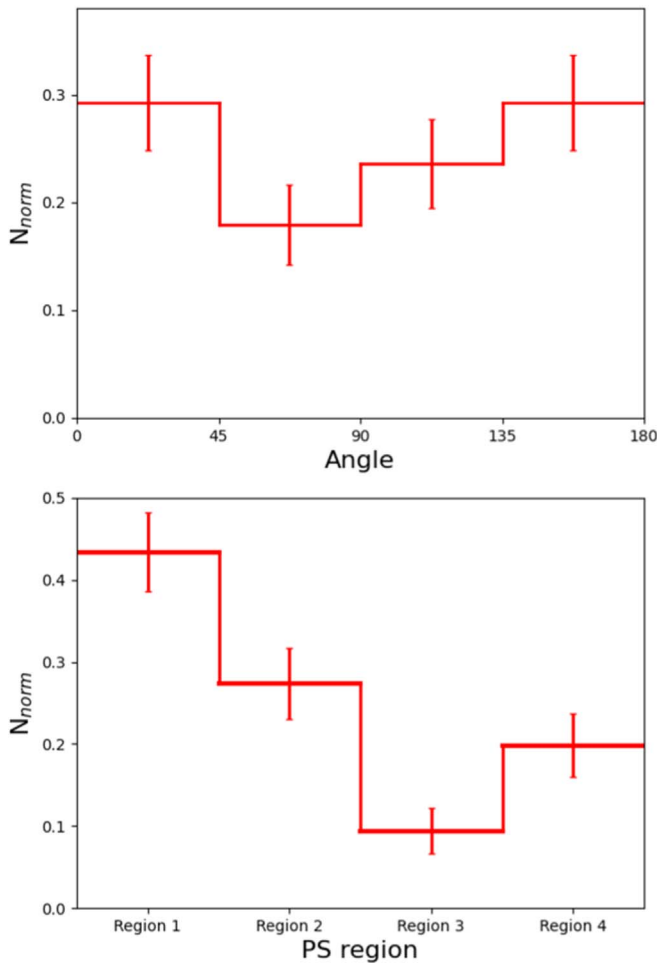
Figure 8. Tail angle and PS region distributions of the main sample of LOFAR JFs. Top panel: the tail angle distribution (the angle between the JF tail and the host center), Bottom panel: the distribution of the JF galaxies in the four PS regions we consider (the regions are illustrated in Figure 5). Uncertainties based on bootstrapping are shown as the error bars.

Figure 9. Results of the MCMC sampling for the main LOFAR JF sample. The panels are arranged as described in the Figure 6 caption. In summary, for the main LOFAR sample, tails typically initially appear when the first-infaller galaxies reach about three-quarters of the host's r_{200}, and they last for several hundred Myr after the galaxy passes orbital pericenter. The poorer constraints on the delay parameter indicate that the results are less sensitive to this parameter.

uncertainties (defined as the width of the 68% credible interval divided by the median) for $r1/r_{200}$, δ, and $t2$ are 0.11, 0.98, and 0.46, respectively, which are similar to the relative uncertainties measured in Section 4 for the two mock tests. Using the simulations, we measure that the median time for a first infaller to reach 76% of r200 is 334 +206 −153 Myr.

In summary, the takeaway message from modeling the full LOFAR sample of JF galaxies is that, for the ensemble of JF galaxies as a whole, their tails typically appear on first infall, when the objects reach roughly three-quarters of the r_{200} of their host, and their tails survive the first pericenter, remaining visible for a few hundred Myr after the pericenter passage. A few hundred Myr is roughly the expected timescale for 144 Mhz radio continuum to decay in a ∼microGauss magnetic field. However, the magnetic field strengths in the tails are quite uncertain, and also the timescales could be increased by the presence of star formation in the tails or decreased if mixing strongly dilutes the tails.

5.2. Subsamples of the Main LOFAR JF Sample

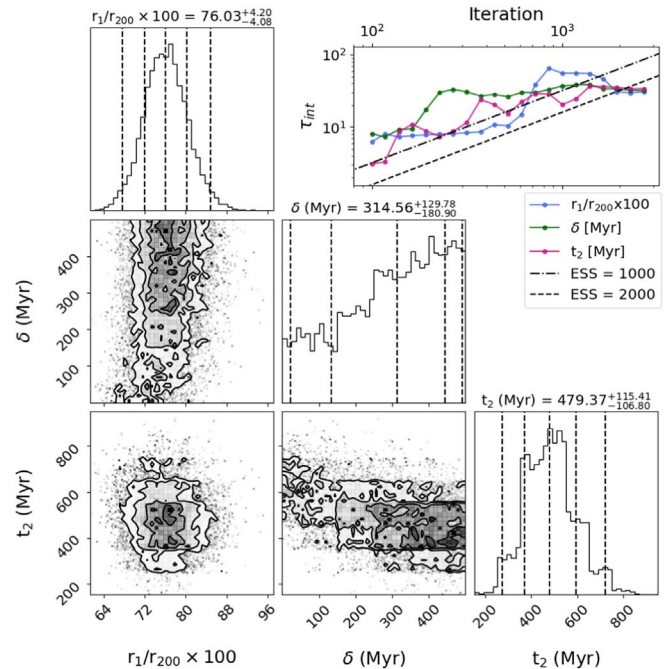The main LOFAR JF sample is a mixture of different mass hosts and different mass satellites (see Figure 1). More massive hosts might be expected to submit their satellites to more powerful ram pressures through a denser ICM and faster orbital velocities. Similarly, lower-mass satellites are expected to be more sensitive to those environmental effects (Gullieuszik et al. 2020). Therefore, in the following, we split our main sample in half, into two equal-sized subsamples,[10] according to host mass (split at $10^{14}\,M_\odot$), galaxy stellar mass (split at $10^{10.2}\,M_\odot$), and the ratio of the satellite to host mass (split at a ratio of 1.5×10^{-4}). The resulting distributions of the tail angles and locations in PS are shown in Appendix C (Figure 13).

We then carry out our analysis on each subsample individually. The PDFs for all three parameters are shown as violin plots in Figure 10. The horizontal dashed line shows the median and the dotted lines encompass the 68% credible interval (the full set of median and 68% credible interval values are additionally provided in Table 2). For comparison purposes, the results for the main sample are shown first, on the left. Besides comparing the PDFs by eye, we also sample from the PDFs one million times, and compute the percentage probability that the value drawn from the PDF of the "Hi" subsample is greater than the value drawn from the PDF of the "Lo" subsample ($P_{\rm H I>Lo}$; the values shown in lower left corners of each subsample panel). In this way, for identical distributions, we expect $P_{\rm H I>Lo} = 50\%$; if $P_{\rm H I>Lo} \gg 50\%$, then the "Hi" subsample PDF strongly prefers higher values compared to the "Lo" subsample, and if $P_{\rm H I>Lo} \ll 50\%$, then the "Hi" subsample PDF strongly prefers lower values compared to the "Lo" subsample. We confirm that the $P_{\rm H I>Lo}$ values shown do not change if we were to sample the PDFs in excess of one million times.

---

[10] We also repeated this test using a more extreme upper third versus lower third percentile, and found qualitatively consistent, albeit more noisy, results (due to reduced statistics).
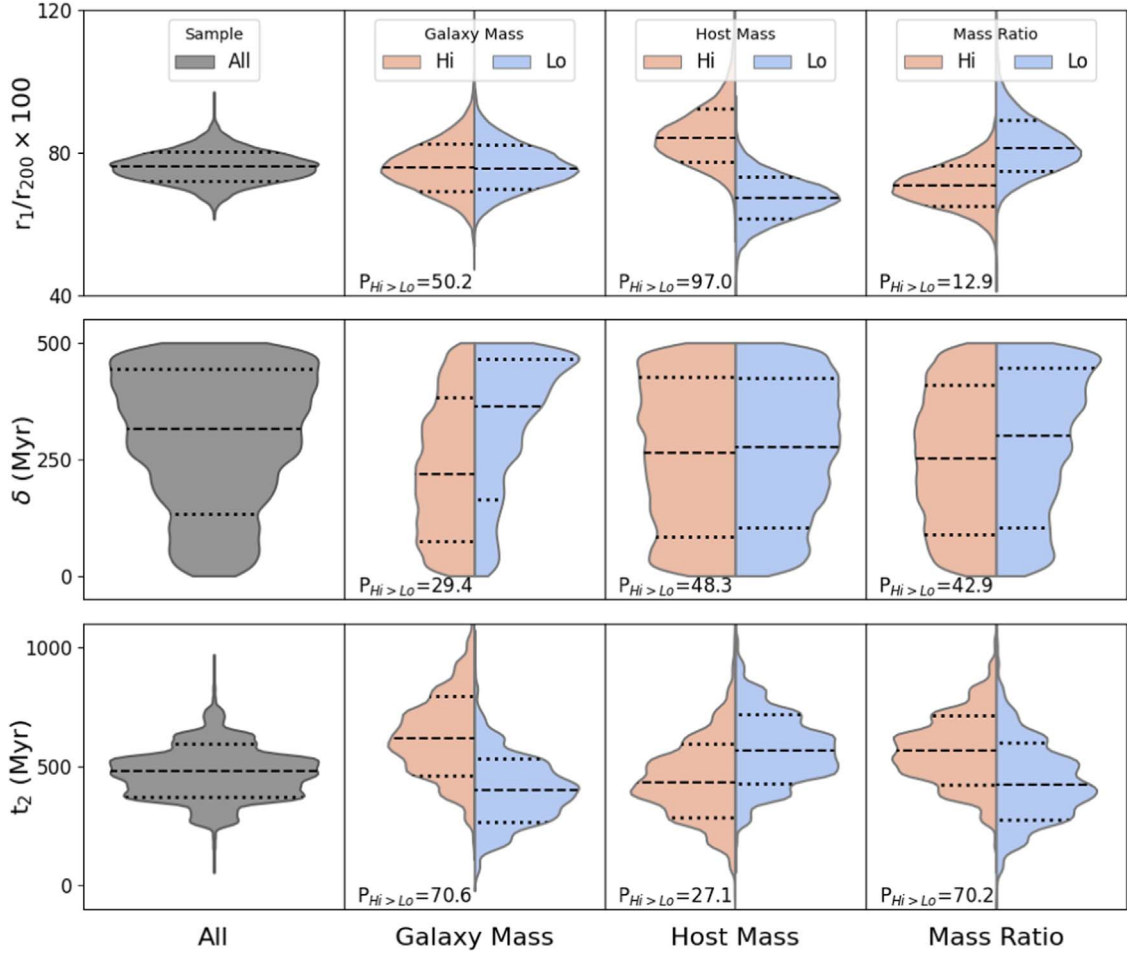
Figure 10. The results of the MCMC sampling for the various subsamples of the main LOFAR JF sample that we consider. The PDFs are shown as violin plots, where the horizontal dashed line is the median and the surrounding dotted lines encompass the 68% credible interval. On the far left, we show a single violin plot for the total sample in gray. Then, we show violin plots for each subsample (from left to right: galaxy stellar mass, host mass, and satellite-to-host mass ratio), where the violin color indicates whether the subsample was the upper or lower half of the sample. Higher host masses and smaller mass ratios cause the tails of the first-infaller galaxies to initially appear further out from the host's center. Lower galaxy masses, lower mass ratios, or higher host masses cause the tails to disappear more quickly after pericenter. The $P_{\rm H\,I>Lo}$ value (shown in the lower left corner of each subsample panel) is the percentage probability that the parameter for the "Hi" subsample is greater than the one for the "Lo" subsample (see the text for further details).

Table 2
The Results of the MCMC Sampling for the Various Subsamples of the Main LOFAR JF Sample (as Illustrated Visually in Figure 10)

Sample	$100 \times r_1/r_{200}$	δ (Myr)	$t2$ (Myr)
All	$76.0^{+4.2}_{-4.1}$	$314.6^{+129.8}_{-180.9}$	$479.4^{+115.4}_{-106.8}$
Hi Galaxy Mass	$75.7^{+6.9}_{-6.6}$	$218.2^{+163.6}_{-144.3}$	$618.7^{+176.3}_{-154.6}$
Lo Galaxy Mass	$75.7^{+6.5}_{-5.7}$	$363.5^{+103.0}_{-198.9}$	$398.0^{+136.8}_{-132.2}$
Hi Host Mass	$84.2^{+8.1}_{-6.7}$	$262.9^{+163.2}_{-179.9}$	$433.5^{+164.0}_{-147.1}$
Lo Host Mass	$67.4^{+5.8}_{-5.8}$	$275.3^{+149.6}_{-172.0}$	$566.8^{+153.9}_{-136.6}$
Hi Mass Ratio	$70.7^{+5.9}_{-5.5}$	$250.7^{+159.2}_{-161.6}$	$564.6^{+149.3}_{-139.0}$
Lo Mass Ratio	$81.3^{+8.1}_{-6.5}$	$300.7^{+146.4}_{-196.9}$	$423.0^{+177.3}_{-144.6}$

Note. The values given in each cell of the table are the median and the 68% credible interval values of the marginalized PDF for each subsample (format: median ± credible interval).

Moving from left to right, we consider the various subsamples in turn.

Galaxy Mass. $r1/r_{200}$ shows negligible change between the subsamples ($P_{\rm H\,I>Lo} \approx 50\%$). But the median $t2$ is larger for the high-mass satellites (618 Myr) than for the low-mass satellites (398 Myr), and they differ by more than their 68% credible intervals, with $P_{\rm H\,I>Lo} = 70.6\%$. Physically, this means that the moment at which the tails start to become visible is not sensitive to galaxy mass, but more massive galaxies maintain their tails for longer after pericenter passage. This could perhaps be the result of galaxies having similar self-gravity in the outskirts of their disks when the tails first form. But stronger self-gravity near the centers of massive disks could perhaps enable them to hold onto their gas for longer (Jaffé et al. 2018). Or the presence of larger quantities of gas overall in more massive disks could also play a role in extending their visibility after pericenter, as they do not need to lose such large fractions of their disk gas to make a visible tail. We confirm that the median host mass changes negligibly between the galaxy mass subsamples. Lower-mass galaxies tend to have a longer δ parameter (363 Myr) than higher-mass galaxies (218 Myr), although the medians fall inside of each other's 68% credible interval, and $P_{\rm H\,I>Lo} = 29.4\%$, which is a moderate difference compared to the other subsamples.

Host Mass. Unlike with galaxy mass, $r1/r_{200}$ clearly depends on the host mass, with more massive hosts causing the galaxy tails to appear farther out from the host's center (at

84% of r_{200}, compared to 67% for low-mass hosts). The difference between their two PDFs is the largest that we find among our subsamples, with $P_{\rm H I > Lo} = 96.9\%$, and no overlap between their 68% credible intervals. Physically, we interpret this as more massive hosts causing stronger ram pressures in their outskirts, perhaps due to a denser ICM in the outskirts and/or higher infall velocities. Meanwhile, higher-mass hosts also cause a lower $t2$ parameter (434 Myr, compared to 567 Myr for lower-mass hosts). With $P_{\rm H I > Lo} = 27.1\%$, the difference is of a similar order to that shown between the galaxy mass subsamples. This is consistent with the idea that high-mass hosts also have stronger ram pressures near pericenter, which can remove the tails more rapidly following pericenter. We confirm that the median galaxy mass changes negligibly between the subsamples. Meanwhile, the δ parameter distribution does not show significant differences between the subsamples, with $P_{\rm H I > Lo} \approx 50\%$.

Mass Ratio. As with the host mass, both $r1/r_{200}$ and $t2$ show a dependency on the mass ratio. Lower mass ratios cause the tails to appear farther out (the median $r1/r_{200}$ is 81%, compared to 71% for the higher mass ratio, differing by more than the 68% credible limit) and to disappear more quickly after pericenter ($t2$ is 423 Myr, compared to 565 Myr for the higher mass ratio). The dependency of $r1/r_{200}$ on mass ratio is strong, with $P_{\rm H I > Lo} = 13.0\%$. For comparison, $t2$ has $P_{\rm H I > Lo} = 70.3\%$, which is of a similar order to the $P_{\rm H I > Lo}$ of the galaxy and host mass subsamples. A lower mass ratio would be expected to cause the galaxy to be more sensitive to ram pressure, as either its stellar mass would be lower or it would be in a more massive host (or both), and hence the appearance of the tail farther out, and its disappearance more quickly after pericenter, does make physical sense. As with the host mass, the δ parameter distribution does not show large differences between the mass ratio subsamples ($P_{\rm H I > Lo} = 42.9\%$).

5.3. Caveats

One caveat of our modeling is we assume that only the orbit through the main host halo can dictate the visibility and direction of the JF tails. This neglects the possibility that some of the observed JF tails could have formed through interactions with the hot gaseous halos of substructures in the outskirts of the hosts. We do not expect this to be a major issue, as the amount of contamination of this type must be generally quite low—our sample contains many group-mass hosts whose substructures must be even lower-mass, and low-mass groups of galaxies are known to have very low JF fractions (<5%; R21b). However, the contamination may be higher in more massive hosts, especially in the case of very irregular hosts, but even in this case we can expect that their tails would tend to be quite randomly oriented with respect to the main host's center. Therefore, when multiple hosts are combined together, they would be unlikely to bias the overall shape of the projected tail angle distribution. We also confirmed that excluding infaller halos that enter the main host as the satellite of another more massive halo had a negligible effect on the projected tail angle distribution.

Another caveat is that some of our observed JF tails may be the result of tidal interactions with a nearby companion galaxy. Best efforts were made to exclude obvious cases of tidally interacting galaxies in R21a and R21b, but it is not possible to fully rule out this possibility. Nevertheless, we would expect that such objects would have tail directions that are primarily a

function of the orbital interactions with their neighbors, and thus quite randomly oriented with respect to the host center. Thus, as with substructure, their presence would be unlikely to alter the overall shape of the tail angle distribution.

An alternative issue is that some galaxies that undergo ram pressure suffer the unwinding of their spiral structure (Bellhouse et al. 2021), and these morphological features are frequently observed in populations of blue cluster galaxies (Vulcani et al. 2022). In this case, simulations have revealed that their tails do not always point exactly downwind of their disks, if the stripped material was previously rotating rapidly, and especially if their disks are viewed face-on. However, as we use wide angle bins (with a width of 45°), and because the observed galaxy disks will be viewed with a range of inclinations, we can expect this to be a mild source of noise in the tail angle distribution, without significantly modifying its overall shape.

We emphasize that the median values of $r1$, δ, and $t2$ that we recover for a galaxy sample should be considered typical values for the ensemble of galaxies as a whole, but individual galaxies in the sample may differ from these values considerably, according to other parameters that we have so far marginalized over (e.g., the density of the ICM or the dynamical state of the host). It would be interesting to test additional parameters in the future, beyond those that we have considered so far (host mass, galaxy mass, and mass ratio). It may be difficult to apply our method to clusters that are actively undergoing major mergers, where the cluster center is poorly defined and the galaxy orbits and dynamics of the ICM may be highly perturbed (McPartland et al. 2016; Roman-Oliveira et al. 2019). We also add that the reliability of our results will depend on whether JF galaxies actually do follow the model's prescription of a tail appearing at $r1$ and then remaining visible until $t2$, as currently assumed.

Finally, we note that our choice of the boundaries between the PS regions was fairly arbitrary, so it may be possible to improve the constraints even further by adjusting the locations of the regions in future works. Nevertheless, our tests with the mocks (e.g., see Figure 7 and the discussions in the main text) reveal that the chosen regions already provide valuable constraints.

6. Conclusions

In this study, we present a new and original method for constraining where the tails of observed JF galaxies appear and how long they last for following their orbital pericenter. We demonstrate our approach on a sample of 106 JF galaxies identified in LoTSS, which exist inside 68 hosts, such as groups and clusters. In star-forming galaxies, LoTSS is sensitive to synchrotron emission from cosmic rays accelerated by supernovae. For star-forming galaxies experiencing ram pressure stripping, tails of synchrotron emission may be observed, as these cosmic rays are stripped from their star-forming galactic disks. We measure the distribution of their tail angles with respect to the stellar mass–weighted host centers. We also measure their distribution into regions of a PS plot of hostcentric line-of-sight velocity versus projected radius. We then compare these two observed distributions (tail angles and PS regions) to predictions from models based on cosmological simulations. The novelty of our approach is to "paint on" the JF tails onto the dark matter halos of our N-body cosmological simulations, using a three-parameter model ($r1$, δ, $t2$) to decide at which radius the tails first become visible ($r1$ as a percentage

of the host's r_{200}), how long the tails are visible for after pericenter passage ($t2$ in Myr), and a delay parameter (δ in Myr) that accounts for the delay in the tail directions to respond to rapid changes in orbital direction. In this way, we can quickly cover a large area of parameter space, and produce distributions of the projected tail angles and the locations in PS regions for comparison with the observations. The model is also highly flexible, and thus the tail properties are not limited by treatments of hydrodynamical processes and subgrid physics that could artificially influence our results. Based on a Bayesian parameter estimation using the MCMC method, we obtain the PDFs of the parameters ($r1$, δ, $t2$) for our observed sample.

Our main results can be summarized as follows.

1. Tests with mock observational data sets that have similar uncertainties as in our observed sample demonstrate that our method can provide useful constraints on both $r1$ and $t2$, when the distributions of both the angle bins and PS regions are combined. δ is not found to be an influential parameter for controlling the shape of the distributions.

2. Applying the method to the full sample of 106 LOFAR JF galaxies, the Bayesian parameter estimation returns PDFs with median values of $r1 = (76.0^{+4.2}_{-4.1})\%$, $t2 = (479.4^{+115.4}_{-106.8})$ Myr, and $\delta = (314.6^{+129.8}_{-180.9})$ Myr, where the limits encompass the 68% credible interval. Thus, tails typically appear shortly after the satellites have crossed the host's r_{200} for the first time, and the tails survive the first pericenter passage and are still visible several hundred Myr later.

3. We split the full sample of LOFAR JFs in half, into two equal-sized subsamples, according to satellite mass, host mass, and the mass ratio of the satellite to the host. In general, we find that satellites that would be expected to be more influenced by ram pressure (e.g., those in more massive hosts or with lower masses with respect to their host) tend to present tails farther out in the host and also lose their tails more quickly after pericenter.

This study demonstrates that our novel approach to modeling the observed tail directions of JFs and their locations in PS can provide useful physical constraints on where JF tails first appear, and highlight the interesting result that typically JF galaxies display visible radio-continuum tails even after having passed pericenter. The implications of this are interesting, as we can assume that the peak strength of the ram pressure occurs at the time of pericenter. Therefore, the presence of visible tails at later times could imply that gas that was stripped near pericenter has not yet fully separated from the galaxy. As the ram pressure strength may rapidly drop following pericenter, in principle some of this gas might even fall back onto the disks.

Our sample was visually selected by the presence of JF tails, as seen in the radio continuum, and, as such, the parameter estimation can be considered valid for our sample. However, this parameter estimation may not be valid for a more general sample of infalling late-type galaxies, because there will likely be additional parameters (for example, gas fraction) that decide whether they form tails like those visible in our sample. In the near future, we will apply this method to alternative data sets, including samples of JF tails identified at other wavelengths, such as optical (e.g., Poggianti et al. 2016; Roberts & Parker 2020; Hyper Suprime-Cam imaging, Galaxy Zoo), H I (e.g., VIVA, Meerkat, Wallaby), Ultraviolet (e.g., Galex,

UVIT), or Hα (e.g., VESTIGE, GASP, INT) imaging. The different components of a galaxy are expected to respond in different ways to ram pressure. For example, the atomic gas component as traced by 21 cm may be stripped earliest, as it is more extended, but the tails may quickly disappear if they are ionized. Other tracers may only be seen if there has been recent star formation in the tails (e.g., UV). Hα can arise either from star formation or other mechanisms, such as shocks or ICM–interstellar medium interactions (Poggianti et al. 2019c; Campitiello et al. 2021). Therefore, the time when tails appear and how long they last for could be sensitive to the tracer that is considered. We expect that the application of our novel method to alternative data sets could provide new insights into the formation and survival of JF tails, and the physical processes occurring within them.

Appendix A
Noise Tests

As described in Section 2.1, for our main LOFAR JF sample, we choose to cut our sample for all galaxies where the background noise level is greater than 200 μJy beam^{-1}. In this section, we consider how our results would change if we had chosen a more strict 150 μJy beam^{-1} cut. Figure 11 shows violin plots of the PDFs for the $r1$ (upper row), δ (middle row), and $t2$ (lower row) of the various subsamples that we consider in Section 5.2. The central long-dashed line indicates the median, while the surrounding short-dashed lines encompass the 50% credible interval. The darker-colored histograms are our standard noise cut of 200 μJy beam^{-1}, while the paler histogram shows the more strict noise cut of 150 μJy beam^{-1}. Overall, the results are similar, and all agree within the 50% credible interval. When comparing high to low galaxy mass, host mass, or mass ratio subsamples, the general dependency on that parameter is conserved. This demonstrates that our main conclusions on where tails become visible and how long they last for, and their general dependencies on these parameters, are robust to the levels of noise in our main sample.
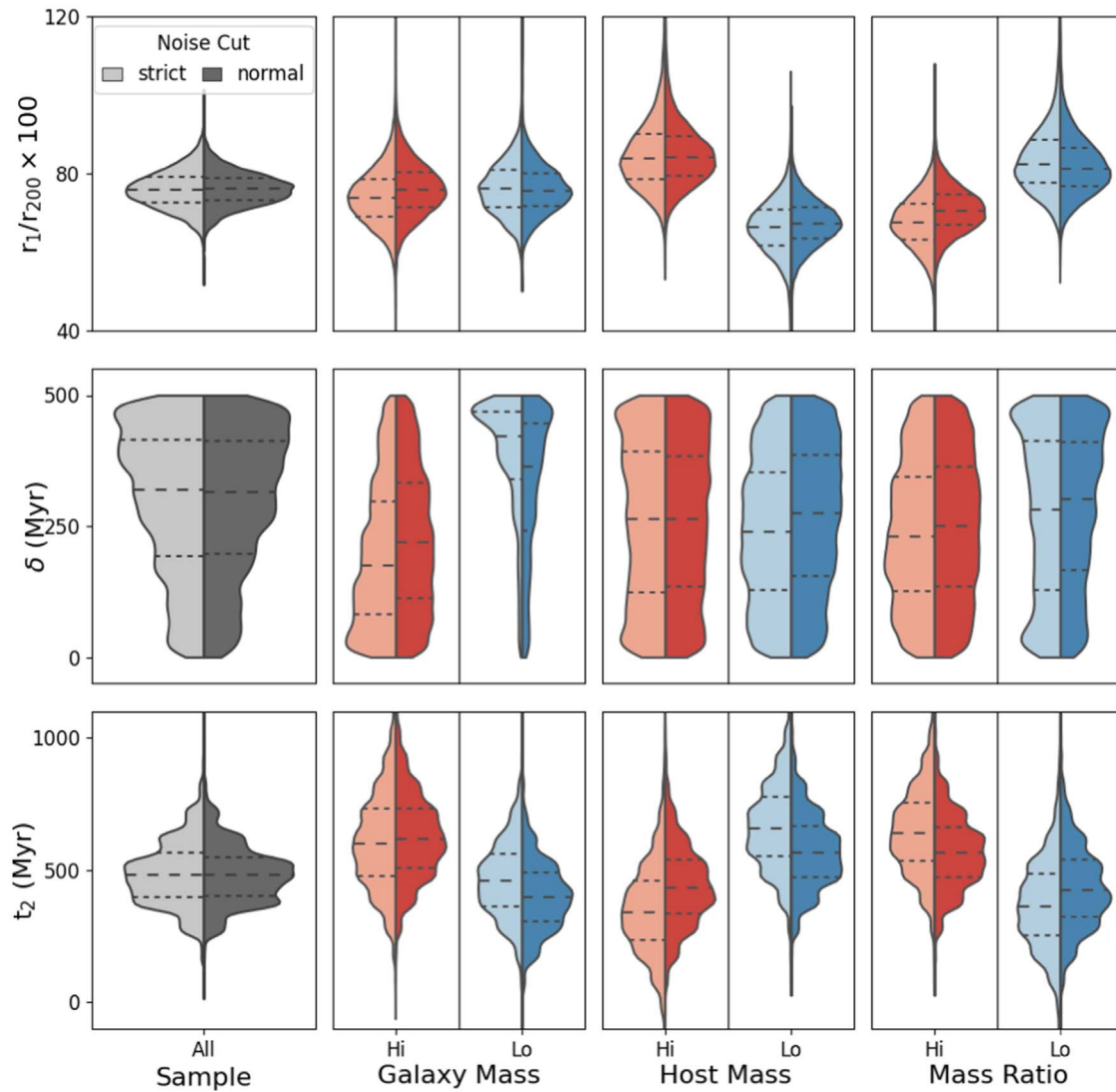
Figure 11. The results of the MCMC sampling for two different choices of noise cut. The marginalized PDFs of each parameter are shown as violin plots. 200 μJy beam^{-1} is our standard noise cut value (the darker-colored histogram; labeled "normal"), and is compared to the more strict value of 150 μJy beam^{-1} (the lighter-colored histogram; labeled "strict"). The results are similar overall and the medians (shown as the horizontal long-dashed lines) agree within the 50% credible interval (shown as the horizontal short-dashed lines).

Appendix B
Properties of Galaxies Split by Tail Direction

The red histograms in Figure 12 are tails pointing away from the host's center. As an additional test, we split our main LOFAR JF sample into two subsamples, based on the direction of their tails with respect to their host's center. The red histograms are tails pointing away from the host's center (tail angle >90°, labeled "Away," containing 50 galaxies), and the blue histograms point toward it (tail angle <90°, labeled "Toward," containing 56 galaxies). We can expect that the "Toward" subsample will have more objects that have passed pericenter than the "Away" sample (which is reasonable, as illustrated in Figure 4).

We see from the distribution shapes and the median lines that the "Away" sample appears to prefer higher-mass hosts, lower-mass galaxies, and lower mass ratios (the first three panels, from left to right). In the main paper, galaxies with higher-mass hosts, lower masses, and lower mass ratios tend to lose their tails more quickly (a shorter $t2$) and/or form their tails earlier (a larger $r1$), as shown in Figure 10, thus they might be expected to prefer the "Away" sample. Therefore, the results shown here seem to offer support for the results in the main paper.

The fourth histogram (on the far right) shows the asymmetry distribution of the subsamples (as defined in Equation (1)). We see that the "Toward" subsample prefers smaller asymmetry values, which could be interpreted as them having shorter tails after passing pericenter. Physically, this could occur because the ram pressure would be expected to decrease in strength after passing pericenter. Additionally, 144 Mhz radio-continuum emission is expected to fade on timescales of hundreds of Myrs, as the synchotron-emitting electrons age and the emission shifts to lower frequencies, in the absence of any reacceleration in the tail (Feretti & Giovannini 2008).

However, we add a note of caution. Although some of the differences between the red and blue histograms in each panel are visible by eye, according to a Kolmogorov–Smirnov (KS) test, the differences between the red and blue histograms in each panel are not very significant. If D is the KS statistic and p is the corresponding p-value, we measure $(D, p) = (0.228, 0.13)$ for host mass, $(0.183, 0.34)$ for galaxy mass, $(0.204, 0.22)$ for mass ratio, and $(0.156, 0.48)$ for asymmetry, so all the p-values are greater than 0.05. The poor number statistics (∼50 galaxies in each subsample) likely contribute to the low significance of these results. This emphasizes the value of our modeling in the main paper, which shows diverse distinctions between the various parameters (see Figure 10) in a way that the test presented here cannot.
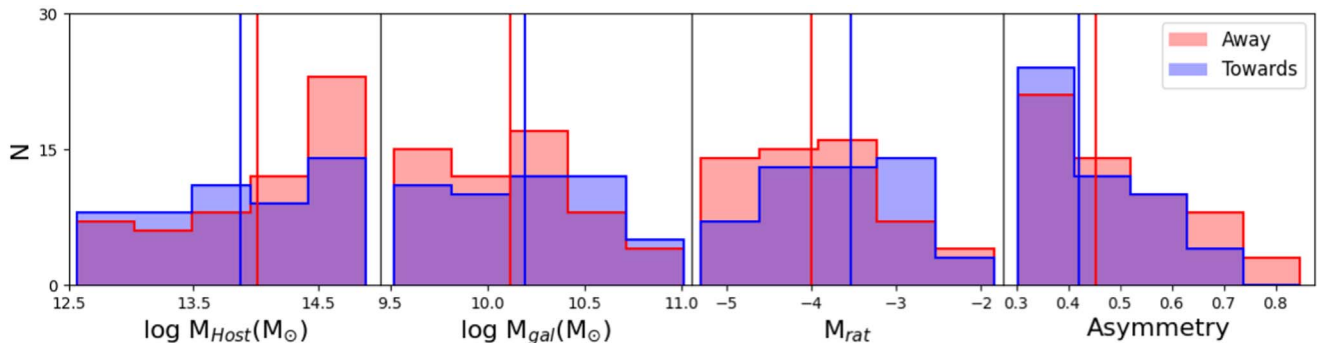

Figure 12. Our main LOFAR JF sample is split into two subsamples by the directions of their tails (red is pointing away from and blue is pointing toward the host's center). The histograms compare the properties (host mass, galaxy mass, mass ratio, and asymmetry, shown from left to right, respectively) of the two subsamples. The vertical lines indicate the median values of the distributions.
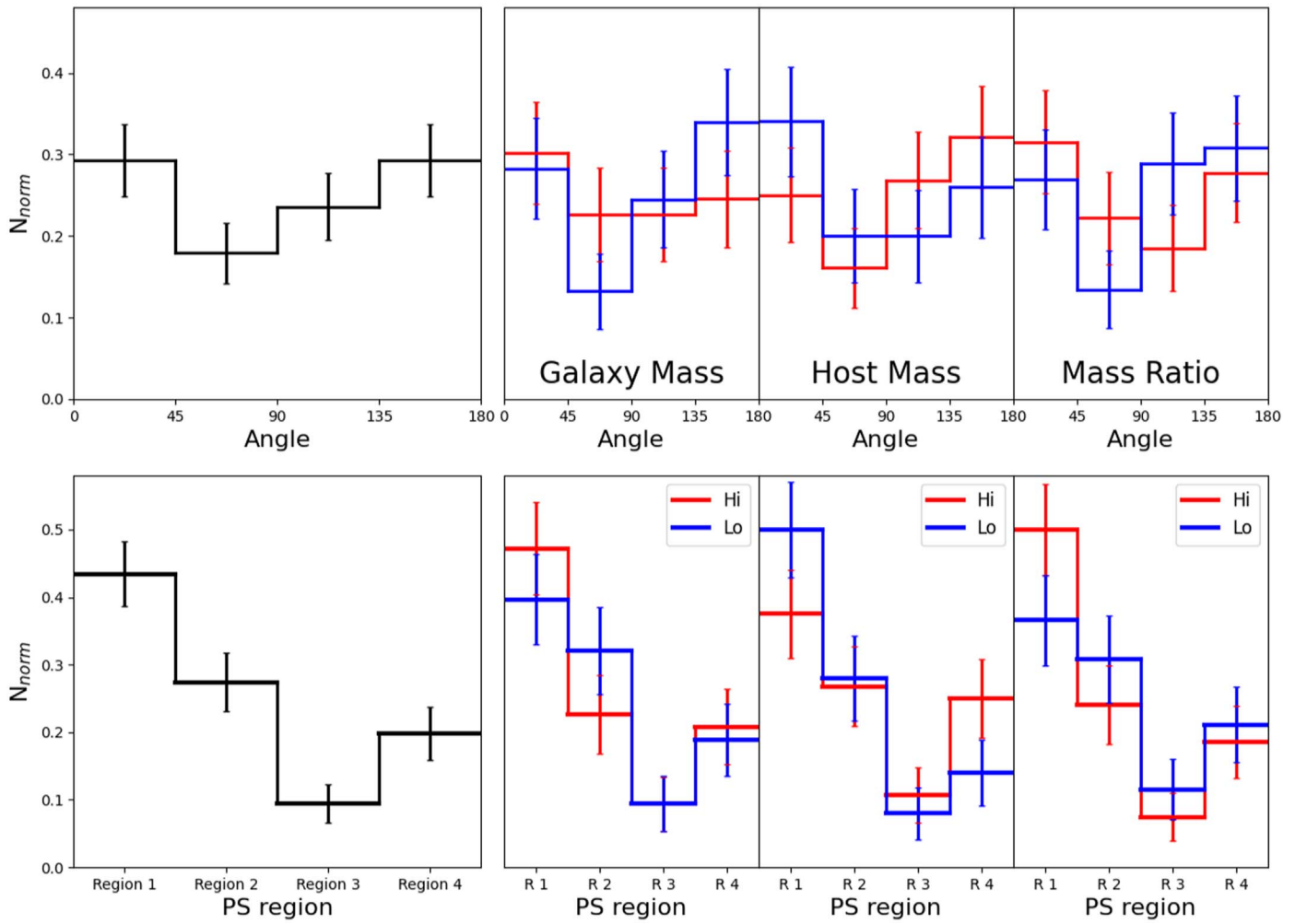
Figure 13. Histograms of the observed tail angle distribution (top row) and the locations of the samples in the PS regions (bottom row), for the main LOFAR JF sample (first column) and for the high (red) and low (blue) subsamples, which split the main sample according to galaxy mass, host mass, and mass ratio (columns 2 to 4, respectively). Uncertainties based on bootstrapping are shown as the error bars.

Appendix C
Histograms of the LOFAR JF Subsamples

As described in Section 5.2, our main LOFAR JF subsample is split into high and low subsamples, according to galaxy stellar mass (split at $10^{10.2}\,M_\odot$), host mass (split at $10^{14}\,M_\odot$), and the ratio of the satellite to host mass (split at a ratio of 1.5×10^{-4}). The impact on the shapes of the histograms can be seen in Figure 13. These histograms are then used as the input for our method, and the resulting PDFs of the three model parameters r_1, δ, and t_2, can be seen in Figure 10.

ORCID iDs

Rory Smith ⬥ https://orcid.org/0000-0001-5303-6830
Jong-Ho Shinn ⬥ https://orcid.org/0000-0001-7967-6473
Stephanie Tonnesen ⬥ https://orcid.org/0000-0002-8710-9206
Paula Calderón-Castillo ⬥ https://orcid.org/0000-0002-7069-113X
Yara L. Jaffe ⬥ https://orcid.org/0000-0003-2150-1130
Ian Roberts ⬥ https://orcid.org/0000-0002-0692-0911
Sean McGee ⬥ https://orcid.org/0000-0003-3255-3139
Koshy George ⬥ https://orcid.org/0000-0002-1734-8455
Benedetta Vulcani ⬥ https://orcid.org/0000-0003-0980-1499
Marco Gullieuszik ⬥ https://orcid.org/0000-0002-7296-9780
Alessia Moretti ⬥ https://orcid.org/0000-0002-1688-482X
Bianca M. Poggianti ⬥ https://orcid.org/0000-0001-8751-8360
Jihye Shin ⬥ https://orcid.org/0000-0001-5135-1693

References

Abadi, M. G., Moore, B., & Bower, R. G. 1999, MNRAS, 308, 947
Abramson, A., Kenney, J., Crowl, H., & Tal, T. 2016, AJ, 152, 32
Bahé, Y. M., & McCarthy, I. G. 2015, MNRAS, 447, 969
Bahé, Y. M., McCarthy, I. G., Balogh, M. L., & Font, A. S. 2013, MNRAS, 430, 3017
Behroozi, P. S., Wechsler, R. H., Wu, H.-Y., et al. 2013, ApJ, 763, 18
Bellhouse, C., Jaffé, Y. L., McGee, S. L., et al. 2019, MNRAS, 485, 1157
Bellhouse, C., McGee, S. L., Smith, R., et al. 2021, MNRAS, 500, 1285
Boquien, M., Burgarella, D., Roehlly, Y., et al. 2019, A&A, 622, A103
Boselli, A., Fossati, M., & Sun, M. 2022, A&ARv, 30, 3
Boselli, A., & Gavazzi, G. 2006, PASP, 118, 517
Boselli, A., Cuillandre, J. C., Fossati, M., et al. 2016, A&A, 587, A68
Boselli, A., Fossati, M., Ferrarese, L., et al. 2018, A&A, 614, A56
Botteon, A., van Weeren, R. J., Brunetti, G., et al. 2020, MNRAS, 499, L11
Bravo-Alfaro, H., Cayatte, V., van Gorkom, J. H., & Balkowski, C. 2000, AJ, 119, 580
Bravo-Alfaro, H., Cayatte, V., van Gorkom, J. H., & Balkowski, C. 2001, A&A, 379, 347
Brown, T., Catinella, B., Cortese, L., et al. 2017, MNRAS, 466, 1275

Campitiello, M. G., Ignesti, A., Gitti, M., et al. 2021, ApJ, 911, 144
Cayatte, V., Kotanyi, C., Balkowski, C., & van Gorkom, J. H. 1994, AJ, 107, 1003
Cayatte, V., van Gorkom, J. H., Balkowski, C., & Kotanyi, C. 1990, AJ, 100, 604
Chamaraux, P., Balkowski, C., & Gerard, E. 1980, A&A, 83, 38
Chen, H., Sun, M., Yagi, M., et al. 2020, MNRAS, 496, 4654
Chung, A., van Gorkom, J. H., Kenney, J. D. P., Crowl, H., & Vollmer, B. 2009, AJ, 138, 1741
Chung, A., van Gorkom, J. H., Kenney, J. D. P., & Vollmer, B. 2007, ApJL, 659, L115
Cortese, L., Catinella, B., & Smith, R. 2021, PASA, 38, e035
Cortese, L., Marcillac, D., Richard, J., et al. 2007, MNRAS, 376, 157
Cortese, L., Ciesla, L., Boselli, A., et al. 2012, A&A, 540, A52
Cowie, L. L., & Songaila, A. 1977, Natur, 266, 501
Cramer, W. J., Kenney, J. D. P., Sun, M., et al. 2019, ApJ, 870, 63
Cramer, W. J., Kenney, J. D. P., Tonnesen, S., et al. 2021, ApJ, 921, 22
Davé, R., Rafieferantsoa, M. H., & Thompson, R. J. 2017, MNRAS, 471, 1671
Davies, R. D., & Lewis, B. M. 1973, MNRAS, 165, 231
De Lucia, G., Hirschmann, M., & Fontanot, F. 2019, MNRAS, 482, 5041
Deb, T., Verheijen, M. A. W., Gullieuszik, M., et al. 2020, MNRAS, 494, 5029
Dénes, H., Kilborn, V. A., & Koribalski, B. S. 2014, MNRAS, 444, 667
Donnari, M., Pillepich, A., Nelson, D., et al. 2021, MNRAS, 506, 4760
Durret, F., Chiche, S., Lobo, C., & Jauzac, M. 2021, A&A, 648, A63
Ebeling, H., Stephenson, L. N., & Edge, A. C. 2014, ApJL, 781, L40
Emerick, A., Mac Low, M.-M., Grcevich, J., & Gatto, A. 2016, ApJ, 826, 148
Feretti, L., & Giovannini, G. 2008, in A Pan-Chromatic View of Clusters of Galaxies and the Large-Scale Structure, ed. M. Plionis, O. López-Cruz, & D. Hughes, Vol. 740 (Dordrecht: Springer), 24
Finn, R. A., Desai, V., Rudnick, G., et al. 2018, ApJ, 862, 149
Foreman-Mackey, D., Hogg, D. W., Lang, D., & Goodman, J. 2013, PASP, 125, 306
Foreman-Mackey, D., Farr, W., Sinha, M., et al. 2019, JOSS, 4, 1864
Fossati, M., Gavazzi, G., Savorgnan, G., et al. 2013, A&A, 553, A91
Fossati, M., Mendel, J. T., Boselli, A., et al. 2018, A&A, 614, A57
Fumagalli, M., Gavazzi, G., Scaramella, R., & Franzetti, P. 2011, A&A, 528, A46
Gavazzi, G., Boselli, A., Cortese, L., et al. 2006, A&A, 446, 839
Gavazzi, G., Boselli, A., Pedotti, P., Gallazzi, A., & Carrasco, L. 2002, A&A, 396, 449
Gavazzi, G., Consolandi, G., Gutierrez, M. L., Boselli, A., & Yoshida, M. 2018, A&A, 618, A130
Gavazzi, G., Fumagalli, M., Fossati, M., et al. 2013, A&A, 553, A89
Ge, C., Sun, M., Liu, R.-Y., et al. 2019, MNRAS, 486, L36
George, K., Poggianti, B. M., Gullieuszik, M., et al. 2018, MNRAS, 479, 4126
Gnedin, O. Y. 2003, ApJ, 582, 141
Grishin, K. A., Chilingarian, I. V., & Afanasiev, A. V. 2021, NatAs, 5, 1308
Gronke, M., Oh, S. P., Ji, S., & Norman, C. 2022, MNRAS, 511, 859
Gullieuszik, M., Poggianti, B. M., Moretti, A., et al. 2017, ApJ, 846, 27
Gullieuszik, M., Poggianti, B. M., McGee, S. L., et al. 2020, ApJ, 899, 13
Gunn, J. E., & Gott, J. R. I. 1972, ApJ, 176, 1
Hahn, O., & Abel, T. 2011, MNRAS, 415, 2101
Haynes, M. P., & Giovanelli, R. 1986, ApJ, 306, 466
Healy, J., Blyth, S. L., Verheijen, M. A. W., et al. 2021, A&A, 650, A76
Hester, J. A. 2010, ApJ, 720, 191
Huchtmeier, W. K., Tammann, G. A., & Wendker, H. J. 1976, A&A, 46, 381
Jáchym, P., Sun, M., Kenney, J. D. P., et al. 2017, ApJ, 839, 114
Jaffé, Y., Smith, R., Candlish, G. N., et al. 2015, MNRAS, 448, 1715
Jaffé, Y. L., Poggianti, B. M., Moretti, A., et al. 2018, MNRAS, 476, 4753
Jones, M. G., Espada, D., Verdes-Montenegro, L., et al. 2018, A&A, 609, A17
Jung, S. L., Choi, H., Wong, O. I., et al. 2018, ApJ, 865, 156
Kazantzidis, S., Mayer, L., Callegari, S., Dotti, M., & Moustakas, L. A. 2017, ApJL, 836, L13
Kennicutt, R. C. 1983, ApJ, 272, 54
Koopmann, R. A., Haynes, M. P., & Catinella, B. 2006, AJ, 131, 716
Koopmann, R. A., & Kenney, J. D. P. 2004a, ApJ, 613, 851
Koopmann, R. A., & Kenney, J. D. P. 2004b, ApJ, 613, 866
Lal, D. V. 2020, ApJS, 250, 22
Lewis, A., Challinor, A., & Lasenby, A. 2000, ApJ, 538, 473
Lim, S. H., Mo, H. J., Lu, Y., Wang, H., & Yang, X. 2017, MNRAS, 470, 2982
Liu, Q., Yee, H. K. C., Drissen, L., et al. 2021, ApJ, 908, 228
Loni, A., Serra, P., Kleiner, D., et al. 2021, A&A, 648, A31
Lotz, M., Remus, R.-S., Dolag, K., Biviano, A., & Burkert, A. 2019, MNRAS, 488, 5370
Marasco, A., Crain, R. A., Schaye, J., et al. 2016, MNRAS, 461, 2630

McPartland, C., Ebeling, H., Roediger, E., & Blumenthal, K. 2016, MNRAS, 455, 2994
Merrifield, M. R. 1998, MNRAS, 294, 347
Minchin, R. F., Taylor, R., Köppen, J., et al. 2019, AJ, 158, 121
Moore, B., Ghigna, S., Governato, F., et al. 1999, ApJL, 524, L19
Moore, B., Katz, N., Lake, G., Dressler, A., & Oemler, A. 1996, Natur, 379, 613
Müller, A., Poggianti, B. M., Pfrommer, C., et al. 2020, NatAs, 5, 159
Muzzin, A., van der Burg, R. F. J., McGee, S. L., et al. 2014, ApJ, 796, 65
Nulsen, P. E. J. 1982, MNRAS, 198, 1007
Oman, K. A., & Hudson, M. J. 2016, MNRAS, 463, 3083
Oosterloo, T., & van Gorkom, J. 2005, A&A, 437, L19
Owen, F. N., Keel, W. C., Wang, Q. D., Ledlow, M. J., & Morrison, G. E. 2006, AJ, 131, 1974
Owers, M. S., Couch, W. J., Nulsen, P. E. J., & Rand all, S. W. 2012, ApJL, 750, L23
Pasquali, A., Smith, R., Gallazzi, A., et al. 2019, MNRAS, 484, 1702
Pawlik, M. M., Wild, V., Walcher, C. J., et al. 2016, MNRAS, 456, 3032
Poggianti, B. M., Fasano, G., Omizzolo, A., et al. 2016, AJ, 151, 78
Poggianti, B. M., Moretti, A., Gullieuszik, M., et al. 2017, ApJ, 844, 48
Poggianti, B. M., Gullieuszik, M., Tonnesen, S., et al. 2019, MNRAS, 482, 4466
Poggianti, B. M., Ignesti, A., Gitti, M., et al. 2019c, ApJ, 887, 155
Ramatsoku, M., Serra, P., Poggianti, B. M., et al. 2019, MNRAS, 487, 4580
Reiprich, T. H., Basu, K., Ettori, S., et al. 2013, SSRv, 177, 195
Rhee, J., Smith, R., Choi, H., et al. 2017, ApJ, 843, 128
Roberts, I. D., & Parker, L. C. 2020, MNRAS, 495, 554
Roberts, I. D., van Weeren, R. J., McGee, S. L., et al. 2021a, A&A, 652, A153
Roberts, I. D., van Weeren, R. J., Timmerman, R., et al. 2022, A&A, 658, A44
Roberts, I. D., van Weeren, R. J., McGee, S. L., et al. 2021b, A&A, 650, A111
Roediger, E., & Brüggen, M. 2007, MNRAS, 380, 1399
Roman-Oliveira, F. V., Chies-Santos, A. L., Rodríguez del Pino, B., et al. 2019, MNRAS, 484, 892
Rose, J. A., Robertson, P., Miner, J., & Levy, L. 2010, AJ, 139, 765
Salim, S., Boquien, M., & Lee, J. C. 2018, ApJ, 859, 11
Salim, S., Lee, J. C., Janowiecki, S., et al. 2016, ApJS, 227, 2
Scott, T. C., Bravo-Alfaro, H., Brinks, E., et al. 2010, MNRAS, 403, 1175
Sharma, S. 2017, ARA&A, 55, 213
Shimwell, T. W., Röttgering, H. J. A., Best, P. N., et al. 2017, A&A, 598, A104
Shimwell, T. W., Tasse, C., Hardcastle, M. J., et al. 2019, A&A, 622, A1
Shinn, J.-H. 2020, MNRAS, 499, 1073
Smith, R., Duc, P. A., Candlish, G. N., et al. 2013, MNRAS, 436, 839
Smith, R., Sánchez-Janssen, R., Beasley, M. A., et al. 2015, MNRAS, 454, 2502
Smith, R. J., Lucey, J. R., Hammer, D., et al. 2010, MNRAS, 408, 1417
Solanes, J. M., Giovanelli, R., & Haynes, M. P. 1996, ApJ, 461, 609
Solanes, J. M., Manrique, A., García-Gómez, C., et al. 2001, ApJ, 548, 97
Springel, V., Yoshida, N., & White, S. D. M. 2001, NewA, 6, 79
Stevens, A. R. H., Diemer, B., Lagos, C. d. P., et al. 2019, MNRAS, 483, 5334
Sun, M., Donahue, M., & Voit, G. M. 2007, ApJ, 671, 190
Sun, M., Ge, C., Luo, R., et al. 2021, NatAs, 6, 270
Tak, H., Ghosh, S. K., & Ellis, J. A. 2018, MNRAS, 481, 277
Tonnesen, S. 2019, ApJ, 874, 161
Tonnesen, S., & Bryan, G. L. 2009, ApJ, 694, 789
Tonnesen, S., & Stone, J. 2014, ApJ, 795, 148
Toribio, M. C., Solanes, J. M., Giovanelli, R., Haynes, M. P., & Martin, A. M. 2011, ApJ, 732, 93
Troncoso-Iribarren, P., Padilla, N., Santander, C., et al. 2020, MNRAS, 497, 4145
Valluri, M., & Jog, C. J. 1990, ApJ, 357, 367
Valluri, M., & Jog, C. J. 1991, ApJ, 374, 103
Vijayaraghavan, R., & Sarazin, C. 2017, ApJ, 848, 63
Vollmer, B. 2003, A&A, 398, 525
Vollmer, B., Balkowski, C., Cayatte, V., van Driel, W., & Huchtmeier, W. 2004, A&A, 419, 35
Vollmer, B., Cayatte, V., Balkowski, C., & Duschl, W. J. 2001, ApJ, 561, 708
Vulcani, B., Poggianti, B. M., Smith, R., et al. 2022, ApJ, 927, 91
Vulcani, B., Poggianti, B. M., Gullieuszik, M., et al. 2018a, ApJL, 866, L25
Vulcani, B., Poggianti, B. M., Jaffé, Y. L., et al. 2018b, MNRAS, 480, 3152
Vulcani, B., Poggianti, B. M., Tonnesen, S., et al. 2020, ApJ, 899, 98
Wang, J., Staveley-Smith, L., Westmeier, T., et al. 2021, ApJ, 915, 70
Wang, L., Yang, X., Shen, S., et al. 2014, MNRAS, 439, 611

Warmels, R. H. 1988, A&AS, 72, 427

Wood, R. A., Jones, C., Machacek, M. E., et al. 2017, ApJ, 847, 79

Xie, L., De Lucia, G., Hirschmann, M., & Fontanot, F. 2020, MNRAS, 498, 4327

Yagi, M., Yoshida, M., Gavazzi, G., et al. 2017, ApJ, 839, 65

Yagi, M., Yoshida, M., Komiyama, Y., et al. 2010, AJ, 140, 1814

Yoon, H., Chung, A., Smith, R., & Jaffé, Y. L. 2017, ApJ, 838, 81

Yoshida, M., Yagi, M., Komiyama, Y., et al. 2008, ApJ, 688, 918

Yun, K., Pillepich, A., Zinger, E., et al. 2019, MNRAS, 483, 1042

Zinger, E., Dekel, A., Kravtsov, A. V., & Nagai, D. 2018, MNRAS, 475, 3654

Zoldan, A., De Lucia, G., Xie, L., Fontanot, F., & Hirschmann, M. 2017, MNRAS, 465, 2236